Riemann wave description of erosional dam-break flows

By L. FRACCAROLLO[1] and H. CAPART[2]†

[1]Dipartimento di Costruzioni e Tecnologia Avanzata, Università di Messina,
and Dipartimento di Ingegneria Civile e Ambientale, Università degli Studi di Trento, Italy

[2]Department of Civil Engineering, Université catholique de Louvain,
and Fonds National de la Recherche Scientifique, Belgium

This work examines the sudden erosional flow initiated by the release of a dam-break wave over a loose sediment bed. Extended shallow-water equations are formulated to describe the development of the surge. Accounting for bed material inertia, a transport layer of finite thickness is introduced, and a sharp interface view of the morphodynamic boundary is adopted. Approximations are sought for an intermediate range of wave evolution, in which equilibration of the sediment load can be assumed instantaneous but momentum loss due to bed friction has not yet been felt. The resulting homogeneous hyperbolic equations are mathematically tractable using the Riemann techniques of gas dynamics. Dam-break initial conditions give rise to self-similar flow profiles. The wave structure features piecewise constant states, two smoothly varied simple waves, and a special type of shock: an erosional bore forming at the forefront of the wave. Profiles are constructed through a semi-analytical procedure, yielding a geomorphic generalization of the Stoker solution for dam-break waves over rigid bed. For most flow properties, the predictions of the theoretical treatment compare favourably with experimental tests visualized using particle imaging techniques.

1. Introduction

Propagating over a loose sediment substrate, water surges may in some circumstances set in motion significant amounts of bed material. A static granular medium saturated with water can be driven to join the flow as a rapidly deforming solid–liquid mixture. Such bulking with eroded material may in turn significantly affect the wave dynamics. Not only does sediment entrainment influence the surge by modifying its rheological behaviour and remoulding its underlying topography, but for rapidly varying conditions, the bulking process itself exerts a strong feedback on the wave through incorporation of bed material inertia. Erosional transients of this kind are encountered in various conditions of geomorphological and engineering interest. These include valley forming floods (Lapointe *et al.* 1998; Brooks & Lawrence 1999), debris surges in mountainous terrain (Takahashi 1991; Iverson 1997) and sheet-flow sediment entrainment in the coastal surf and swash zones (Asano 1995; Sumer *et al.* 1996).

The present work addresses an extreme occurrence of such phenomena, that is, the erosional flow resulting from the sudden release of a dam-break wave over a mobile sediment bed. The configuration considered is shown on figure 1. A horizontal

† Present address: Department of Civil Engineering, National Taiwan University, Taiwan.
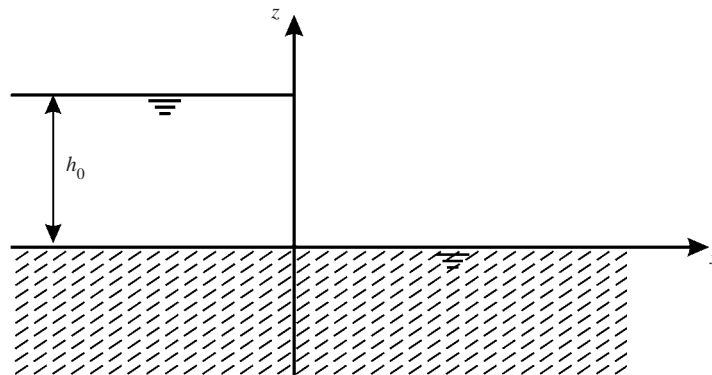
FIGURE 1. Initial conditions for the erosional dam-break wave. A horizontal bed of loose water-saturated sediments extends upstream and downstream of an idealized dam. The water body of depth h_0 retained upstream is instantaneously released at time $t = 0$ by the dam collapse.

bed composed of coarse, cohesionless sediments saturated with water extends on both sides of an idealized dam. Upstream lies a motionless body of pure water, having depth h_0 above the sediment bed surface. An intense flow of water and eroded sediment is then released by the instantaneous collapse of the dam. The analysis will seek to characterize the hydrodynamic and geomorphic effects which shape the resulting wave structure.

Focus on the geomorphic dam-break problem is motivated by practical, theoretical and experimental considerations. From a practical point of view, first, geomorphic dam-break waves constitute significant hazards in upland valleys. In a number of catastrophes of ancient and recent history, floods from dam failures have been recorded to induce severe soil movements in the form of flowslides, debris waves and sediment-laden currents (Costa & Schuster 1988). A well-documented recent event is the Lake Ha! Ha! break-out flood which occurred in 1996 in the Saguenay region of Québec (Lapointe *et al.* 1998; Brooks & Lawrence 1999). Under heavy rains, lake waters overtopped and swept away a small saddle dyke 1 m in height, then went on to scour a 14 m thick layer of underlying soil, incising a deep channel upstream and downstream of the dyke site (figure 2). Beyond these near-field effects, the flood wave released by the new outlet caused extensive erosion and damage in the downstream valley, locally widening the river course by up to 280 m. Geomorphic effects were strong enough to preclude application of purely hydrodynamic flood routeing procedures (INRS-Eau 1997). Although the idealized dam configuration of figure 1 constitutes only a very rough analogue of the Ha! Ha! cut-away dyke, it will be seen to lead to similar near-field geomorphic effects. The analysis will also point out some inherent limitations of hydrodynamic or alluvial hydraulic descriptions of such extreme events.

The second motivation is theoretical. The geomorphic dam-break problem constitutes a particularly transparent example of more general processes. For the same reason, the rigid bed dam-break problem has become a touchstone of shallow-water theory. The Ritter (1892) and Stoker (1957) analytical solutions for pure water dam-break waves clarify the hydrodynamics of rapid transients. They are also extensively used for the development and validation of computational schemes (e.g. Fennema & Chaudhry 1987; Glaister 1988; Alcrudo, Garcia-Navarro & Saviron 1992; Toro 1992; Fraccarollo & Toro 1995). Under certain assumptions, the erosional dam-break wave is shown in the present work to be amenable to a similar analytical treatment. This
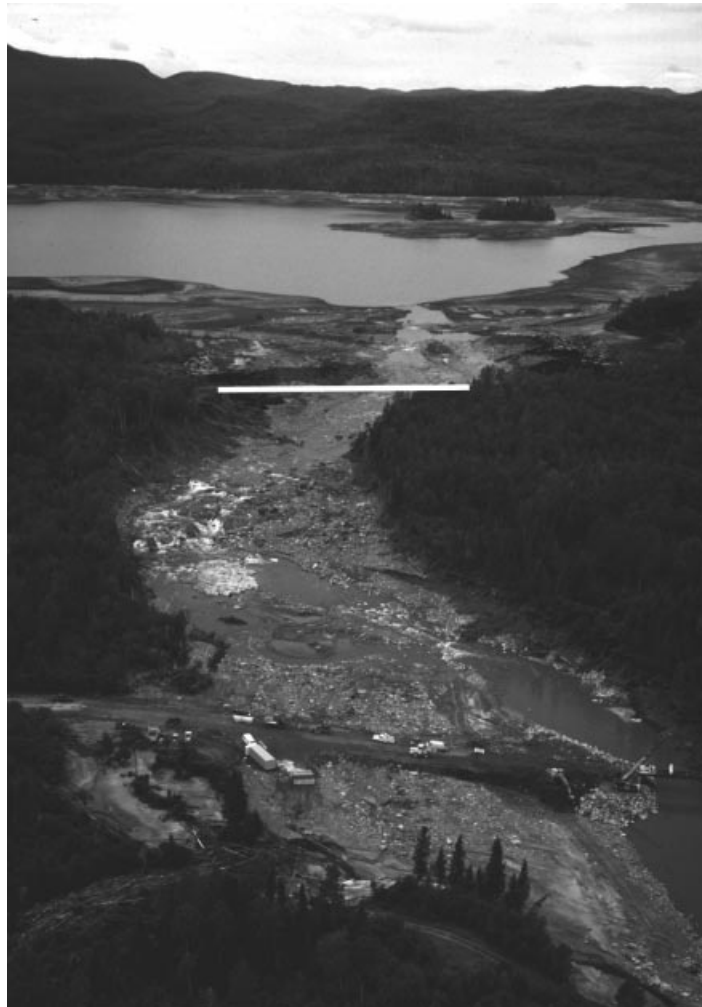
FIGURE 2. 1996 Lake Ha! Ha! break-out flood, Saguenay, Québec. View of the outlet channel scoured by flood waters after overtopping of a small saddle dyke. Original position of the dyke shown in white. The drained lake is shown in the background. Heavy scour progressed both upstream and downstream of the failed dyke (Brooks & Lawrence 1999). Photograph courtesy of Dr G. R. Brooks, Geological Survey Canada.

generalization of the Stoker solution, it is hoped, will prove equally helpful in gaining physical insight and guiding computational efforts.

The third motivation is experimental. The configuration shown in figure 1 is particularly simple to implement in the laboratory. The chief obstacle to erosional dam-break flow experiments lies in their rapid character and high-sensitivity to intruding elements (such as sediment samplers or probes). The burden is thus shifted to measurement techniques. Recent developments in imaging methods (for a review of fluid mechanics applications, see Adrian 1991) provide new solutions to this problem. These were used by Capart and Young (1998) to obtain detailed measurements of mobile bed dam-break experiments performed with very light grains (barely heavier than water). In the present work, we present some new experiments carried out with denser sediment material and improved imaging algorithms.

Severe erosional floods are well documented in the geomorphological literature (Clague, Evans & Blown 1985; Gallino & Pierson 1985; Jarrett & Costa 1986; Waythomas *et al.* 1996; Benito, Grodek & Enzel 1998). To date, fewer studies have been devoted to the mechanics of such processes, prompting this assessment by Costa & Schuster (1988): 'This problem of bulking and debulking of flood flows represent a difficult unsolved problem in sediment transport today, and its consequences for hazard evaluation are significant.' An early laboratory study was carried out by Chen & Simons (1979), who described qualitatively the effects of a dam-break flow on an erodible valley. Laboratory experiments focusing on idealized conditions were performed by Capart & Young (1998), and Leal & Ferreira (1999). These two works also include computational simulations, obtained by extending shallow-water solvers to mobile bed conditions. The equations solved were not established in a systematic fashion, however, and were not analysed in depth from a more mathematical perspective.

In what follows, we will lay out an appropriate set of constitutive assumptions and construct a tractable mathematical description of sudden erosional flows. The proposed view departs from classical alluvial hydraulic treatments (e.g. de Vries 1965; Holly & Rahuel 1990; Zanré & Needham 1994; Saiedi 1997) in that the thickness of the sediment transport layer as well as its inertia cannot be neglected. A discrete system approach (Abbott 1979) is adopted, whereby the flow in the vertical plane is approximated by regions of homogenous properties separated by sharp interfaces. A discontinuity of particular interest is the underlying bed boundary, which we treat as a phase interface across which the saturated sediment material undergoes a transition from solid- to fluid-like behaviour. Proposed by Jenkins & Askari (1991) in the context of kinetic theories of granular flows, such a view will prove extremely useful in the derivation of geomorphic shallow-water equations. These developments are carried out in §2 of the present paper.

A reduced form of the equations is then sought to describe an intermediate time range following the surge release. In this range, equilibration of the sediment load can be assumed instantaneous, while momentum loss due to frictional bed shear is not yet significant. This reduces the mathematical framework to a set of homogeneous hyperbolic equations. The derivation of this approximation and the delineation of its domain of validity are addressed in §3. Riemann solutions to the reduced equations are then constructed in §4. The dam-break initial conditions shown in figure 1 define a Riemann problem from which self-similar profiles emerge. They are formed of piecewise constant states, smooth simple waves and discontinuous shocks, the combination of which is subject to certain compatibility conditions. Once a wave structure is identified, the construction of solutions amounts to the integration of a coupled set of ODEs. This final operation is accomplished with simple numerical quadrature, resolving sharply the jumps and cusps of the flow profile.

The Riemann solutions are finally compared to experimental results in §5. Detailed measurements were obtained for two small-scale laboratory dam-break waves. The first test case was presented in Capart & Young (1998) and features an erosional surge entraining very light bed material. For this case, the results derived previously using manually supervised image analysis methods are complemented by additional measurements obtained with recently developed automated algorithms (Capart, Young & Zech 2002). To approach more closely the conditions of validity of the present theoretical analysis, a new series of tests was further conducted using denser material and a longer observation window. The granular motion acquisition for these tests involves a much larger number of particle tracks, and is performed entirely using

the automated algorithms. The measurements allow a clear visualization of the flow structure, suitable for comparison with the theoretical predictions. After discussion of these results, concluding remarks close the analysis.

2. Geomorphic shallow-water equations

2.1. *Phenomenological assumptions*

Highly erosive free surface flows propagating over loose beds of coarse, cohesionless sediments are considered. Sediment materials of interest range from the light artificial analogues often used in laboratory studies to the heavier sand, gravel or stone materials found in nature. We focus on regimes of intense erosion and sediment transport, well beyond Shields' threshold of individual grain motion. In such regimes, coarse sediments are observed to move collectively as a dense sheet of contact load, many grains thick, occupying a significant portion of the flow depth (Asano 1995; Sumer *et al.* 1996). This transport layer can be entrained by an upper layer composed of mostly clear water. It may also invade the entire flow depth, a condition referred to as mature debris flow (Takahashi 1991). Here, we neglect suspended load, and do not consider conditions in which layers of low sediment concentration may carry a significant sediment flux (Hanes & Bowen 1985).

Four phenomenological assumptions form the basis of the adopted description: (i) shallow water: the surface flow is oriented in a predominantly horizontal direction and is confined to a layer of small thickness relative to the horizontal scale of interest; (ii) effective mixture flow: the heterogeneous liquid–granular flow behaves as an effective medium with little slip between water and transport layers and negligible seepage between fluid and solid phases; (iii) contact load: the sediment phase is mostly transported as contact load, supported by frictional and collisional grain–grain interactions; (iv) morphodynamic interface: the bed boundary is viewed as a phase interface across which the liquid–granular mixture undergoes a transition from solid- to fluid-like behaviour.

These assumptions motivate the following idealization of the vertical flow structure. We postulate the discontinuous system shown on figure 3. Three sharp interfaces are introduced. Interface Γ_w is the air–water boundary at the flow free surface. Interface Γ_s defines the upper limit of the transport layer, separating the clear water layer above from the liquid–granular mixture below. Such a sharp stratification of the flow is motivated by experimental observations (Yeganeh, Bakhtiary & Asano 1998), which indicate a relatively clear boundary between sediment-rich and sediment-free regions in sheet flows of coarse materials. Mature debris flow conditions are obtained when interfaces Γ_w and Γ_s coincide. The third interface Γ_b is the bed boundary, and differs in nature from the other two. Whereas Γ_w and Γ_s are material interfaces passively convected with the flow, active boundary Γ_b is not a material interface. It is modelled as a phase interface across which the water–granular mixture undergoes a discontinuous change of state (Jenkins & Askari 1991). Above the bed interface Γ_b, the liquid–granular mixture is assumed to flow as a fluid, while a solid-like behaviour is considered underneath (i.e. a rigid granular skeleton through which groundwater seepage is neglected). Erosion occurs as boundary Γ_b progresses downwards, and deposition results when the boundary moves up. In both cases, no vertical motion of the material takes place; the material simply liquefies or solidifies as it is traversed by the moving interface. Such a view is supported both by computational simulations (Zhang & Campbell 1992; Aharonov & Sparks 2000)
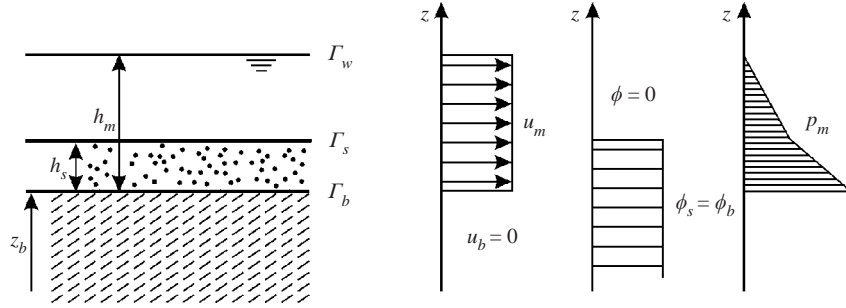
FIGURE 3. Postulated vertical flow structure. From top to bottom: pure water layer; transport layer featuring a flowing mixture of water and grains; water-saturated loose granular substratum. Fluid-like behaviour is assumed for the two upper layers, and solid-like behaviour for the underlying motionless substrate. Interfaces Γ_w, Γ_s and Γ_b are allowed to evolve in time and space.

and by experimental measurements (Capart *et al.* 2000) of the micromechanical behaviour of frictional–collisional granular flows. Its incorporation within a shallow-water framework constitutes the core of the present description.

As shown in figure 3, the three interfaces define separate layers for which we adopt the simplest possible distributions of horizontal velocity and granular concentration: piecewise constant vertical profiles. The heterogeneous flow layer bounded by interfaces Γ_w and Γ_b moves at horizontal mixture velocity u_m assumed uniform over depth h_m. There is no slip between the clear water sublayer and the transport sublayer. Underneath interface Γ_b the solid-like bed material behaves as a rigid body. In a frame of reference at rest, the horizontal bed velocity u_b is equal to zero. An infinitely thin basal shear layer characterized by slip velocity $u_m - u_b$ thus coincides with the bed boundary Γ_b. Consistent with empirical observations, the phase interface between fluid- and solid-like behaviour is embedded within this shear layer.

A similarly idealized distribution is adopted for the granular concentration. The clear-water layer has volumetric solid concentration $\phi = 0$. Underneath interface Γ_s, both the transport layer and the static bed are assumed to exhibit the same granular packing $\phi = \phi_s = \phi_b$. To allow motion, some expansion of the granular phase away from static packing is required. Average volumetric solid fractions are expected to vary from $\phi_b \approx 0.6$ to $\phi_s \approx 0.3$ for sheet-flow (Nnadi & Wilson 1992), and from $\phi_b \approx 0.6$ to $\phi_s \approx 0.5$ for mature debris flow (Armanini *et al.* 2000). This range is small enough to have little effect on the vertical distribution of weight, hence the approximation is retained. In what follows, intermediate value $\phi = \phi_s = \phi_b = 0.5$ is adopted for both layers.

Since vertical accelerations are neglected, the hydrostatic assumption holds in the fluid-like portion of the vertical column. The two fluid-like sublayers are characterized by densities ρ_w and $\rho_w(1 + (s-1)\phi_s) = \rho_w(1 + r)$, where $s = \rho_s/\rho_w$ is the density of the sediment material relative to water, and $r = (s-1)\phi_s$ is the density supplement due to the presence of the sediment load. Both ρ_w and ρ_s are constants as we assume incompressible phases. The vertical pressure distribution within the mixture is therefore as shown in figure 3, with an integral over depth given by

$$\int_{z_b}^{z_w} p_m \, \mathrm{d}z = \rho_w (\tfrac{1}{2} g h_m^2 + \tfrac{1}{2} r g h_s^2), \tag{1}$$

where $h_m = z_w - z_b =$ depth of the flowing layer, and $h_s = z_s - z_b =$ depth of the sediment transport sublayer (here and throughout the paper, unit width is assumed
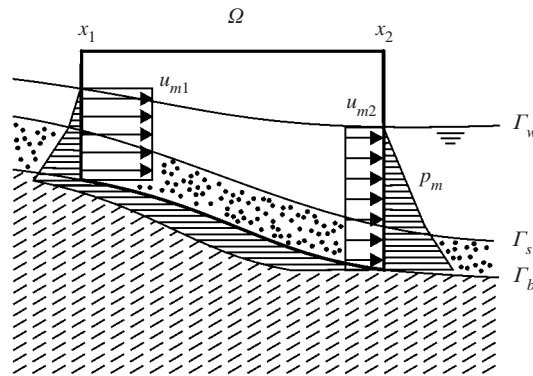
FIGURE 4. Control volume Ω used for the derivation of geomorphic shallow-water equations. The lower boundary of the control volume is fitted to the morphodynamic bed interface Γ_b.

in the transversal y direction). The hydrostatic pressure distribution only applies to fluids, characterized by vanishing shear stress when the medium is at rest. Hence, the assumption does not hold below bed interface Γ_b where the water–granular mixture behaves as a solid. In other words, the stress state within the solid-like bed region is indeterminate. It is shown below how closure of the description can be achieved despite this indeterminancy.

2.2. *Integral equations*

By virtue of the shallow-water assumption, the above vertical structure is taken to hold both for uniform and spatially varied flow. A hydraulic theory then results from the application of continuity and momentum balance principles. Figure 4 shows the special control volume Ω chosen for this purpose. We adopt a frame of reference at rest with respect to the static bed, in which $u_b = 0$. Vertical facets bound the control volume at left-hand and right-hand positions $x_1(t)$ and $x_2(t)$. They are allowed to translate in time at speeds

$$v_1 = \frac{\mathrm{d}x_1}{\mathrm{d}t}, \quad v_2 = \frac{\mathrm{d}x_2}{\mathrm{d}t}, \tag{2a,b}$$

where v is used to distinguish speeds of non-material interfaces (here control volume surfaces) from material velocities u. Freely moving lateral boundaries will be required later to derive shock relations. Placed within the air region above the flow free surface Γ_w, the upper control surface is not traversed by any material flux (we neglect the mass density of air ρ_a).

Specification of the lower boundary is most critical; we constrain it to coincide at all times with portion $\Gamma_{b1,2}$ of the bed interface going from x_1 to x_2. The lower control surface, therefore, moves and deforms along with the bed interface at speed $\boldsymbol{v}_b$. Choice of this special control surface aims at including only fluid-like material inside the control volume. This is required to achieve closure of the momentum balance without having to specify the stress state within the static bed. Determination of internal stresses in the solid-like region would involve the solution of a non-local stress–strain problem, an endeavour outside the scope of the present hydraulic theory.

Applied to the balance of mass and linear momentum in an arbitrarily deforming control volume, the Reynolds transport theorem (e.g. White 1999) yields general

integral equations

$$\frac{\partial}{\partial t} \int_\Omega \rho \, \mathrm{d}\Omega + \int_\Gamma i \, \mathrm{d}\Gamma = 0, \tag{3}$$

$$\frac{\partial}{\partial t} \int_\Omega \rho \boldsymbol{u} \, \mathrm{d}\Omega + \int_\Gamma \boldsymbol{j} \, \mathrm{d}\Gamma = \int_\Omega \rho \boldsymbol{g} \, \mathrm{d}\Omega, \tag{4}$$

where, for continuous fields, the mass and momentum flux densities across control surface Γ are given by

$$i = \rho(\boldsymbol{u} - \boldsymbol{v}) \cdot \boldsymbol{n}, \tag{5}$$

$$\boldsymbol{j} = \rho \boldsymbol{u}((\boldsymbol{u} - \boldsymbol{v}) \cdot \boldsymbol{n}) - \boldsymbol{\sigma} \cdot \boldsymbol{n}, \tag{6}$$

in which ρ = mass density, $\boldsymbol{u}$ = material velocity, $\boldsymbol{v}$ = speed of non-material boundary Γ, $\boldsymbol{n}$ = outward unit normal to Γ, $\boldsymbol{\sigma}$ = stress tensor and $\boldsymbol{g}$ = oriented acceleration due to gravity.

Specializing (3) and (4) to the special control volume of figure 4, we obtain the following integral equations for flow layer continuity, transport layer continuity, and horizontal flow momentum:

$$\frac{\partial}{\partial t} \int_{x_1}^{x_2} h_m \, \mathrm{d}x + [h_m(u_m - v)]_1^2 = \int_{\Gamma_{b1,2}} e_b \, \mathrm{d}\Gamma_b, \tag{7}$$

$$\frac{\partial}{\partial t} \int_{x_1}^{x_2} h_s \, \mathrm{d}x + [h_s(u_m - v)]_1^2 = \int_{\Gamma_{b1,2}} e_b \, \mathrm{d}\Gamma_b, \tag{8}$$

$$\frac{\partial}{\partial t} \int_{x_1}^{x_2} (h_m + r h_s) u_m \, \mathrm{d}x + [(h_m + r h_s) u_m (u_m - v) + \tfrac{1}{2} g h_m^2 + \tfrac{1}{2} r g h_s^2]_1^2 = -\frac{1}{\rho_w} \int_{\Gamma_{b1,2}} j_{bx} \, \mathrm{d}\Gamma_b, \tag{9}$$

where $[f]_1^2 = f(x_2) - f(x_1) = f_2 - f_1$, $e_b = -i_b/(\rho_w(1+r))$ = erosion rate = volume flux density across the evolving bed interface Γ_b and j_{bx} = x-component of the momentum flux density across Γ_b. Conservation of mass applied to the solid bed substrate left out of control volume Ω yields a third continuity equation

$$\frac{\partial}{\partial t} \int_{x_1}^{x_2} z_b \, \mathrm{d}x + [-v z_b]_1^2 = -\int_{\Gamma_{b1,2}} e_b \, \mathrm{d}\Gamma_b. \tag{10}$$

The left-hand sides of (7)–(10) describe rates of change of mass and momentum, as well as the corresponding fluxes across the left-hand and right-hand vertical boundaries. When written in integral form, the classical shallow-water equations (Whitham 1974; Abbott 1979) feature closely analogous terms. Differences stem from the presence here of a transport sublayer of finite thickness h_s, denser than pure water, which contributes to the flow inertia and to the hydrostatic pressure thrust in momentum equation (9).

The right-hand sides of (7)–(10) are most specific to the present geomorphic context. These terms correspond to fluxes across the evolving bed boundary Γ_b. They include all contributions associated with spatial and temporal variations of the bed interface. Because the control surface is fitted to a discontinuity, care must be exercised in evaluating these fluxes. At positions $\boldsymbol{x}$ located along Γ_b, we must distinguish between quantities η^- and η^+ observed on the inner and outer sides:

$$\eta^-(\boldsymbol{x}) = \lim_{\substack{\xi \to 0 \\ <}} \eta(\boldsymbol{x} + \xi \boldsymbol{n}), \quad \eta^+(\boldsymbol{x}) = \lim_{\substack{\xi \to 0 \\ >}} \eta(\boldsymbol{x} + \xi \boldsymbol{n}), \tag{11a, b}$$

where η is an arbitrary flow property. As a consequence, separate evaluations of flux densities e_b and j_{bx} can be made on both sides of Γ_b. For the description to be consistent, both evaluations should be compatible and we must have:

$$e_b = v_{bn} - u_{mn}^- = v_{bn} - u_{bn}^+, \tag{12}$$

$$\begin{aligned} j_{bx} &= \rho_w(1+r)u_m^-(u_{mn}^- - v_{bn}) - (\boldsymbol{\sigma}_m^- \cdot \boldsymbol{n})_x \\ &= \rho_w(1+r)u_b^+(u_{bn}^+ - v_{bn}) - (\boldsymbol{\sigma}_b^+ \cdot \boldsymbol{n})_x, \end{aligned} \tag{13}$$

where superscripts $-$ and $+$ denote states immediately on the inner and outer sides of the discontinuous bed interface Γ_b. These states are sampled within the fluid-like flowing mixture and the solid-like bed region, respectively, hence the superscripts m and b. The subscript pair m, b is redundant with superscript pair $\pm$, yet both are retained temporarily to emphasize the dual character of boundary Γ_b; it is both a shock-like discontinuity featuring a velocity jump and a phase interface separating distinct states of matter. Quantities u_m^- and u_b^+ are the horizontal components of the material velocities on both sides, whereas additional subscript n is used to denote the components u_{mn}^- and u_{bn}^+ of the same velocities in direction $\boldsymbol{n}$ normal to the interface. In a frame of reference at rest, material velocities inside the bed are zero, i.e. $u_b = u_{bn} = 0$. They are retained in (12) and (13) only to highlight the symmetry of the expressions.

To guarantee equivalence between the inner and outer estimates, we must invoke the Rankine–Hugoniot equations (e.g. Chapman 2000) expressing local conservation of mass and balance of vertical and horizontal momentum across a shock-like discontinuity. Specialized to the present case, these can be written:

$$[\rho(u_n - v_{bn})]_-^+ = 0, \tag{14}$$

$$[\sigma_n]_-^+ = 0, \tag{15}$$

$$[\rho u_x(u_n - v_{bn}) - \tau_n n_z]_-^+ = 0, \tag{16}$$

where the vertical component of momentum density is neglected by virtue of the shallow-water assumption, and where σ_n and τ_n are the normal and shear stresses exerted on bed facet $d\Gamma_b$ orthogonal to $\boldsymbol{n}$. Since $[\rho]_-^+ = 0$ across Γ_b, the following relations result:

$$u_{mn}^- = u_{bn}^+ = 0, \tag{17}$$

$$p_m^- = \sigma_{bn}^+, \tag{18}$$

$$e_b = v_{bn} = -\frac{n_z}{\rho_w(1+r)(u_m^- - u_b^+)}(\tau_m^- - \tau_{bn}^+), \tag{19}$$

which can be verified to be sufficient for compatibility of the inner and outer estimates of e_b and j_{bx} in (12) and (13). In (18) and (19), the fluid mixture stress tensor $\boldsymbol{\sigma}_m$ is assumed to reduce to a pressure p_m and a stress τ_m. The same does not hold for the solid stress tensor $\boldsymbol{\sigma}_b$, hence tractions within the bed do depend on the direction $\boldsymbol{n}$ of the facet. By virtue of the hydrostatic assumption, (18) nevertheless implies

$$\sigma_{bn}^+ = p_m^- = \rho_w g(h_m + rh_s), \tag{20}$$

where the right-hand side term is the weight of the overlying column of fluid-like material, as required by hydrostatic balance. The normal stress applied on a facet parallel to the bed in the solid-like region immediately beneath the interface is therefore known.

Equation (19) links the evolution of the bed morphology to the shear stresses experienced at the bed. It can be interpreted in the following way. The speed v_{bn} at which the bed boundary moves into the underlying static substrate is equivalent to the erosion rate e_b. Normal to bed $\boldsymbol{n}$ is oriented downwards, hence $n_z < 0$. Erosion is driven by a difference between entraining shear stress τ_m^- and resisting shear stress τ_{bn}^+ experienced on both sides of the bed interface. Quantity $\rho_w(1 + r)$ is the inertia of the eroded material (both water and sediment) impulsively set in motion as it joins the flowing mixture. Slip velocity $u_m^- - u_b^+$, finally, is the corresponding velocity jump. The relation is similar to the empirical erosion law applied to debris-entraining flood flows by Takahashi & Nakagawa (1994), which also links the erosion rate to a bed shear stress difference. The equation of these authors features an imbalance between instantaneous and equilibrium bed shear stresses, however, equation (19) involves a difference between instantaneous shear stresses acting on both sides of a discontinuity. In the present derivation, furthermore, the inertia factor derives from a Rankine–Hugoniot argument rather than from empirical considerations.

Collecting together the various results, the integral form of geomorphic shallow-water equations (7)–(10) can be written as follows (one of various equivalent formulations):

$$\frac{\partial}{\partial t} \int_{x_1}^{x_2} h_m \, \mathrm{d}x + [h_m(u_m - v)]_1^2 = \int_{\Gamma_{b1,2}} e_b \, \mathrm{d}\Gamma_b, \tag{21}$$

$$\frac{\partial}{\partial t} \int_{x_1}^{x_2} h_s \, \mathrm{d}x + [h_s(u_m - v)]_1^2 = \int_{\Gamma_{b1,2}} e_b \, \mathrm{d}\Gamma_b, \tag{22}$$

$$\frac{\partial}{\partial t} \int_{x_1}^{x_2} z_b \, \mathrm{d}x + [-vz_b]_1^2 = -\int_{\Gamma_{b1,2}} e_b \, \mathrm{d}\Gamma_b, \tag{23}$$

$$\frac{\partial}{\partial t} \int_{x_1}^{x_2} (h_m + rh_s)u_m \, \mathrm{d}x + [(h_m + rh_s)u_m(u_m - v) + \tfrac{1}{2}gh_m^2 + \tfrac{1}{2}rgh_s^2]_1^2$$
$$= -\int_{x_1}^{x_2} \frac{\tau_{bn}}{\rho_w} \mathrm{d}x - \int_{\Gamma_{b1,2}} \frac{\sigma_{bn}}{\rho_w} \mathrm{d}z_b, \tag{24}$$

complemented by morphodynamic interface relations

$$\sigma_{bn} = \rho_w g(h_m + rh_s), \tag{25}$$

$$e_b = -\frac{n_z}{\rho_w(1 + r)u_m}(\tau_m - \tau_{bn}). \tag{26}$$

In rewriting the right-hand side of (24), use was made of geometrical relations $\mathrm{d}x = -n_z \, \mathrm{d}\Gamma_b$ and $\mathrm{d}z_b = n_x \, \mathrm{d}\Gamma_b$. Bed velocity u_b was replaced by its value $u_b = 0$. To simplify notations, superscripts $\pm$ were dropped since they are redundant with subscripts m and b.

Where shocks are absent and the flow is gradually varied, the equations can be further simplified. For a gently sloped bed interface Γ_b,

$$n_z \approx -1, \quad v_{bn} \approx -\frac{\partial z_b}{\partial t}, \quad \mathrm{d}z_b = \frac{\partial z_b}{\partial x}\mathrm{d}x. \tag{27a–c}$$

Integral equations (21)–(24) can then be applied to a fixed control volume of infinitesimal thickness. Setting the vertical boundary velocities equal to zero, i.e. $v_1 = v_2 = 0$

and taking the limit as $x_2 \to x_1$, governing equations are obtained in divergence form:

$$\frac{\partial h_m}{\partial t} + \frac{\partial}{\partial x}(h_m u_m) = e_b, \qquad \frac{\partial h_s}{\partial t} + \frac{\partial}{\partial x}(h_s u_m) = e_b, \qquad \frac{\partial z_b}{\partial t} = -e_b, \qquad (28a\text{--}c)$$

$$\frac{\partial}{\partial t}((h_m + rh_s)u_m) + \frac{\partial}{\partial x}((h_m + rh_s)u_m^2 + \tfrac{1}{2}gh_m^2 + \tfrac{1}{2}rgh_s^2) + g(h_m + rh_s)\frac{\partial z_b}{\partial x} = -\frac{\tau_{bn}}{\rho_w}, \qquad (29)$$

where erosion rate e_b is given by morphodynamic interface relation

$$e_b = \frac{1}{\rho_w(1+r)u_m}(\tau_m - \tau_{bn}). \qquad (30)$$

Note that because of the non-conservative product $g(h_m + rh_s)\partial z_b/\partial x$ in momentum equation (29), the left-hand side of the equations cannot be cast in perfect conservation form.

2.3. *Empirical shear stress functions*

Constitutive relations are required to specify bed shear stresses τ_{bn} and τ_m experienced on both sides of the bed interface Γ_b. They should be functions of the macroscopic quantities characterizing the localized shear layer, and also involve the fluid and granular material properties. The two shear functions can depend on these variables in different ways, however, since they pertain to two distinct states of matter: solid-like and fluid-like. For each of the two states, simple constitutive models can be borrowed from classical soil mechanics and open-channel hydraulics. The combination of such models in (30) will then turn out to yield results consistent with empirical knowledge about granular sheet and debris flows.

Consider first the solid-like lower side of the bed interface. Whereas the stress tensor inside the solid bulk is indeterminate, boundary Γ_b is special because it constitutes a shear surface. Each elementary bed facet $\mathrm{d}\Gamma_b$ can thus be conceived as a failure plane. Along such a facet, the Coulomb law (Lambe & Whitman 1969) governing yield of a rigid assembly of cohesionless grains can be assumed to hold, i.e.

$$\tau_{bn} = \tan\varphi\, \sigma'_{bn}\frac{u_m}{|u_m|}, \qquad (31)$$

where ratio $u_m/|u_m|$ ensures that the resulting traction is oriented against the flow, parameter φ is the friction angle, and σ'_{bn} is the effective normal stress in accordance with Terzaghi's principle (e.g. Lambe & Whitman 1969). Using (20), the effective normal stress σ'_{bn} is given by

$$\sigma'_{bn} = \sigma_{bn} - p_w = \rho_w rgh_s, \qquad (32)$$

where the pore water pressure p_w has been assumed hydrostatic, i.e. $p_w = \rho_w gh_m$. This last assumption hinges on the instantaneous equilibration of pore pressures, valid only for small volumetric variations of the granular phase and a permeability which is not too small (Iverson & LaHusen 1989). For the friction angle, sheet flow data from Daniel (1965) reinterpreted by Nnadi & Wilson (1992) indicate $\tan\varphi \approx 0.5$, which is the value retained hereafter.

Turning to the fluid-like upper side of the bed interface, the intensely sheared liquid–granular mixture is assumed to be in the collisional regime. In that regime, the experiments of Bagnold (1954) and the predictions of kinetic theories (Jenkins & Savage 1983) extrapolated to liquid–granular flows (Jenkins & Hanes 1998) indicate a quadratic dependence of the shear stress with the shear rate. Applying such a relation

to a shear layer of vanishing thickness, we obtain an expression similar to the Chézy equation of open-channel hydraulics (Chow 1973):

$$\tau_w = \rho_s C_f |u_m| u_m = s\rho_w C_f |u_m| u_m, \tag{33}$$

where ρ_s is the density of the grains which exchange momentum through collisions, u_m is the slip velocity characterizing the basal shear layer (since $u_b = 0$), and C_f is a dimensionless friction coefficient. Sheet flow empirical data from various authors analysed by Asano (1995) suggest that a constant C_f accounts reasonably for observed trends in sediment transport rates measured over a wide range of velocities, material sizes and densities. Some scatter remains, however, hence C_f is retained as the single adjustable constant of the present theory. The sheet-flow measurements of Sumer *et al.* (1996) point to a value $C_f \approx 0.007$, whereas a larger value $C_f \approx 0.03$ approximates the debris flow data of Capart *et al.* (2000). Falling within this range, the value $C_f = 0.014$ fits reasonably well the experimental observations reported in §5, both for light and dense grains, and we adopt it for the subsequent computations. It is not expected, however, to constitute a universal constant.

Inserting these various constitutive assumptions into (30), we obtain a result of the form

$$e_b = \frac{\partial h_s}{\partial t} + \frac{\partial}{\partial x}(h_s u_m) = \frac{1}{t_l}(mu_m^2 - h_s), \tag{34}$$

where lag time t_l and mobility coefficient m are given by

$$t_l = \frac{1+r}{r}\frac{|u_m|}{\tan\varphi\, g}, \quad m = \frac{s}{r}\frac{C_f}{\tan\varphi\, g}. \tag{35a,b}$$

Cast as a lag relationship, (34) is simple to interpret: the sediment layer thickness h_s tends asymptotically towards the equilibrium value $h_s^{eq} = mu_m^2$ which balances exactly stresses τ_{bn} and τ_m acting on both sides of the shear layer. Erosion is obtained when the sediment load is below its equilibrium value, whereas deposition results in the opposite case. The lag time is associated with the inertia of the sediment which has to be accelerated or decelerated in order for the bed interface to evolve in time.

Lag relations similar to (34) have been proposed in the context of alluvial hydraulics (Tsubaki & Saito 1967; Galappatti & Vreugdenhil 1985; Armanini & Di Silvio 1988; Phillips & Sutherland 1989). Dimensional arguments led Capart & Young (1998) to apply an equation of the same type to more intense transport in sheet and debris flow modes. Computations on that basis were found to compare reasonably well with dam-break over erodible bed experiments performed with light material. The present derivation endows (34) with a stronger physical basis, showing its intimate link with erosion laws involving shear stress differences. In addition, it establishes a connection between lag time t_l, equilibrium sediment load h_s^{eq}, and the shear stress functions τ_{bn} and τ_m. The resulting description exhibits various other features which match empirical observations. In accordance with the erosional dam-break wave observations of Capart & Young (1998), the formulation preserves the Froude similarity of the original shallow-water equations. Likewise, the scaling of equilibrium sediment discharge $h_s^{eq} u_m$ with the cube of the velocity amplitude u_m fits well sheet-flow measurements obtained for coarse sediments of various sizes and material densities (Ribberink & Al-Salem 1990; Asano 1995).

Together with morphodynamic interface relation (30) and empirical shear stress functions (31) and (33), divergence equations (28) and (29) form a closed system of evolution equations. They constitute a geomorphic extension of the Saint Venant equations of classical hydraulics. Similar systems of equations have been proposed by

a number of authors (Armanini & Di Silvio 1988; Lai 1991; Takahashi & Nakagawa 1994; Hungr 1995; Armanini & Fraccarollo 1997; Capart & Young 1998). The equations derived here on the basis of a sharp interface view differ from previous formulations in the following ways: (i) the transported material occupies a layer of finite thickness within the flow; (ii) a mechanical link is established between the bed shear stresses and the erosion rate. These features are important for the description of geomorphic transients because they determine the effects of bulking and debulking on the flow dynamics. Integral equations (21)–(24), furthermore, allow treatment of shocks within the domain. They constitute a generalization of integral equations proposed by Zanré & Needham (1994) in the context of alluvial hydraulics.

Non-equilibrium equations (28) and (29) can be solved by numerical means (Capart 2000), but they remain too complex for the more analytical treatment sought in the present work. In the following section, therefore, a further reduction of the equations is performed, suitable for application to an intermediate range of development of erosional dam-break waves.

3. Reduction to homogeneous equations

3.1. *Hydrodynamic, geomorphic and frictional time scales*

The system of divergence equations (28) and (29) can be written in vector form as

$$\frac{\partial U}{\partial t} + A(U)\frac{\partial U}{\partial x} = S(U), \tag{36}$$

where

$$U = \begin{pmatrix} h_m \\ h_s \\ z_b \\ q_m \end{pmatrix}, \quad A = \begin{pmatrix} \dfrac{rh_su_m}{h_m+rh_s} & -\dfrac{rh_mu_m}{h_m+rh_s} & 0 & \dfrac{h_m}{h_m+rh_s} \\ -\dfrac{h_su_m}{h_m+rh_s} & \dfrac{h_mu_m}{h_m+rh_s} & 0 & \dfrac{h_s}{h_m+rh_s} \\ 0 & 0 & 0 & 0 \\ gh_m-u_m^2 & r(gh_s-u_m^2) & g(h_m+rh_s) & 2u_m \end{pmatrix},$$

$$S = \begin{pmatrix} e_b \\ e_b \\ -e_b \\ -\dfrac{\tau_{bn}}{\rho_w} \end{pmatrix}. \tag{37a-c}$$

Symbol $U = (h_m h_s z_b q_m)^T$ denotes the vector of dependent variables, $q_m = (h_m+rh_s)u_m$ is the momentum density of the heterogeneous mixture flow, $A(U)$ is the Jacobian matrix and $S(U)$ is the source term vector. Drawing from the operator splitting procedures of computational methods (Strang 1968; Toro 1989; Saurel & Abgrall 1999), (36) can be decomposed into three separate components, each associated with a specific flow process. The flow hydrodynamics are first described by the homogeneous PDE system

$$\frac{\partial U}{\partial t} + A(U)\frac{\partial U}{\partial x} = 0. \tag{38}$$

Geomorphic exchange and frictional momentum loss processes can then be identified with the two ODE systems

$$\frac{\partial U}{\partial t} = G_e(U), \quad \frac{\partial U}{\partial t} = F_e(U), \tag{39a,b}$$

where we have split source vector $S(U)$ into two distinct components $G_e(U)$ and $F_e(U)$ given by:

$$G_e = \begin{pmatrix} e_b \\ e_b \\ -e_b \\ 0 \end{pmatrix} = \frac{1}{\rho_w(1+r)u_m} \begin{pmatrix} \tau_m - \tau_{bn} \\ \tau_m - \tau_{bn} \\ -(\tau_m - \tau_{bn}) \\ 0 \end{pmatrix}, \quad F_e = \begin{pmatrix} 0 \\ 0 \\ 0 \\ -\dfrac{\tau_{bn}}{\rho_w} \end{pmatrix}. \quad (40a,b)$$

For erosional conditions (hence the subscript e), (39a) associated with source vector $G_e(U)$ describes the geomorphic bed change driven by stress difference $\tau_m - \tau_{bn}$. Equation (39b) associated with source vector $F_e(U)$, on the other hand, describes the frictional momentum loss ascribable to residual shear stress τ_{bn}. To examine sudden depositional flows (e.g. a debris surge slumping into a body of water at rest), a different decomposition would be chosen. As the present work examines a purely eroding flow, we do not consider this alternative.

Specific time scales can now be associated with each of the three processes (38) and (39a,b). Subject to Froude similarity, (38) is characterized by the classical hydro-dynamic time scale:

$$t_0 = \left(\frac{h_0}{g} \right)^{1/2}, \quad (41)$$

where h_0 is a characteristic flow depth, e.g. the initial still-water depth behind the dam in the dam-break problem. The shallow-water assumption applies only (Stoker 1957) to a time range

$$t \gg t_0, \quad (42)$$

where time t is measured from the instant of dam collapse.

Turning to the geomorphic process, rearrangement of (39a) is required to isolate the relevant time scale. Notice first that the stress difference $\tau_m - \tau_{bn}$ can be expressed as a function of variables h_m, h_s and q_m. We can then premultiply both sides of (39a) by matrix

$$\begin{pmatrix} 1 & 0 & 1 & 0 \\ 0 & 1 & 1 & 0 \\ 0 & 0 & 0 & 1 \\ \dfrac{\partial(\tau_m - \tau_{bn})}{\partial h_m} & \dfrac{\partial(\tau_m - \tau_{bn})}{\partial h_s} & 0 & \dfrac{\partial(\tau_m - \tau_{bn})}{\partial q_m} \end{pmatrix}, \quad (43)$$

(where differentiation with respect to one variable is carried out with the other variables kept constant) to obtain the diagonal form

$$\frac{\partial}{\partial t} \begin{pmatrix} z_b + h_m \\ z_b + h_s \\ q_m \\ \tau_m - \tau_{bn} \end{pmatrix} = \begin{pmatrix} 0 & 0 & 0 & 0 \\ 0 & 0 & 0 & 0 \\ 0 & 0 & 0 & 0 \\ 0 & 0 & 0 & -t_g^{-1} \end{pmatrix} \begin{pmatrix} z_b + h_m \\ z_b + h_s \\ q_m \\ \tau_m - \tau_{bn} \end{pmatrix}, \quad (44)$$

in which

$$t_g = -\frac{\rho_w(1+r)u_m}{((\partial(\tau_m - \tau_{bn})/\partial h_m) + (\partial(\tau_m - \tau_{bn})/\partial h_s))} \quad (45)$$

is a relaxation time. The first three components of the vector on the left-hand side of (44) are geomorphic invariants, unaffected by erosional incorporation of bed material into the flow. The last component is governed by an evolution equation cast in

canonical relaxation form. Under constitutive assumptions (31) and (33), relaxation time t_g is given by

$$t_g = \frac{(h_m + rh_s)|u_m|}{2sC_f u_m^2 + \dfrac{r\tan\varphi}{1+r}g(h_m + rh_s)}. \tag{46}$$

Time t_g thus constitutes an unambiguous time scale of the geomorphic process. It governs the asymptotic evolution of the flow towards an equilibrium transport state in which $\tau_m = \tau_{bn}$. Erosion increases depths h_m and h_s while leaving the momentum density $q_m = (h_m + rh_s)u_m$ constant. A net decrease in flow velocity u_m and a corresponding dissipation of kinetic energy is thus experienced by the eroding flow. This 'geomorphic' deceleration is entirely due to bulking of the current with bed material of zero momentum, but finite inertia.

In a similar fashion, the frictional system (39*b*) can be rearranged into

$$\frac{\partial}{\partial t}\begin{pmatrix} h_m \\ h_s \\ z_b \\ q_m \end{pmatrix} = \begin{pmatrix} 0 & 0 & 0 & 0 \\ 0 & 0 & 0 & 0 \\ 0 & 0 & 0 & 0 \\ 0 & 0 & 0 & -t_f^{-1} \end{pmatrix}\begin{pmatrix} h_m \\ h_s \\ z_b \\ q_m \end{pmatrix}, \tag{47}$$

i.e. diagonalized in terms of another set of variables, the first three of which constitute frictional invariants, left unaffected by the action of residual shear stress τ_{bn}. The last component is again subject to a relaxation equation, with relaxation time t_f given by

$$t_f = \frac{(h_m + rh_s)|u_m|}{\tan\varphi\, rgh_s}. \tag{48}$$

Time t_f thus provides an unambiguous time scale for the frictional momentum dissipation. Residual stress τ_{bn} is seen in (47) to asymptotically drive the flow towards a state of rest characterized by $q_m = u_m = 0$.

3.2. *Reduced system*

To investigate the intermediate time behaviour of erosional dam-break waves, we approximate governing equations (28)–(29) by the following reduced system

$$\frac{\partial}{\partial t}(z_b + h_m) + \frac{\partial}{\partial x}(h_m u_m) = 0, \tag{49}$$

$$\frac{\partial}{\partial t}(z_b + h_s) + \frac{\partial}{\partial x}(h_s u_m) = 0, \tag{50}$$

$$\frac{\partial}{\partial t}((h_m + rh_s)u_m) + \frac{\partial}{\partial x}((h_m + rh_s)u_m^2 + \tfrac{1}{2}gh_m^2 + \tfrac{1}{2}rgh_s^2) + g(h_m + rh_s)\frac{\partial z_b}{\partial x} = 0, \tag{51}$$

where

$$h_s = h_s^{eq}(u_m) = \mu\frac{u_m^2}{g}, \tag{52}$$

and μ is a non-dimensional sediment mobility constant. The system is obtained by recasting (28) and (29) in terms of the four components of erosional vector, (44). Shear stress difference $\tau_{bn} - \tau_m$ is assumed to be driven infinitely fast towards zero. Under constitutive assumptions (31) and (33), this leads to transport relation (52) expressing locking of the sediment load h_s onto its equilibrium capacity $h_s^{eq}(u_m)$. Finally, momentum dissipation by residual shear stress τ_{bn} is neglected in (51). In

terms of the time scales identified in the preceding paragraph, these approximations imply

$$t_g \ll t \ll t_f. \tag{53}$$

Validity of the reduced equations thus requires a separation of scales between fast geomorphic change and slow momentum dissipation by residual friction. Examination of the circumstances in which condition (53) holds is deferred to the next subsection. Assuming that it does, the key simplification which has been achieved is to reduce the governing equations to a homogeneous system. The right-hand sides of (49)–(51) are equal to zero, hence the equations are satisfied by arbitrary steady uniform states. Because of equilibrium transport constraint (52), furthermore, only three dependent variables are retained among the four degrees of freedom of the original equations. These simplifications are all that is needed to construct solutions to the dam-break problem by means of semi-analytical techniques.

In accordance with Froude similarity, it is easily verified that a non-dimensional form of the equations can be obtained by normalizing all lengths by h_0, velocities by $(gh_0)^{1/2}$, and time by $t_0 = (h_0/g)^{1/2}$. The two material parameters r and μ intervening in system (49)–(52) are given by

$$r(s) = (s-1)\phi_s, \quad \mu(s) = \frac{s}{r}\frac{C_f}{\tan \varphi}, \tag{54a,b}$$

and are both dimensionless functions of the density ratio $s = \rho_s/\rho_w$. For all computations reported in the present paper, the following valves are adopted for the constitutive constants. They have been introduced above but are reported here together for more convenient reference:

$$\phi_s = \phi_b = 0.5, \quad \tan \varphi = 0.5, \quad C_f = 0.014. \tag{55a–c}$$

Density ratio s is thus the only variable material parameter involved in the description.

3.3. *Shock relations*

Under identical approximations, we can specialize integral equations (21)–(24) to the case of a moving shock. Let an isolated discontinuity separating two gradually varied flow regions have position $x_\beta(t)$ and speed

$$v_\beta(t) = \frac{\mathrm{d}x_\beta}{\mathrm{d}t}. \tag{56}$$

Integral equations (21)–(24) can then be applied to a moving control volume straddling the discontinuity. We can furthermore let the thickness of the control volume tend to zero as the two boundaries $x_1(t)$ and $x_2(t)$ approach $x_\beta(t)$ from the left and from the right. This results in the following equations of the Rankine–Hugoniot type:

$$v_\beta = \frac{[h_m u_m]_1^2}{[z_b + h_m]_1^2}, \tag{57}$$

$$v_\beta = \frac{[h_s u_m]_1^2}{[z_b + h_s]_1^2}, \tag{58}$$

$$v_\beta = \frac{[(h_m + rh_s)u_m^2 + \frac{1}{2}gh_m^2 + \frac{1}{2}rgh_s^2]_1^2 + \int_{\Gamma_{b1,2}} g(h_m + rh_s)\mathrm{d}z_b}{[(h_m + rh_s)u_m]_1^2}, \tag{59}$$

where states 1 and 2 are located immediately to the left and to the right of the discontinuity, $h_s = h_s^{eq}(u_m) = \mu u_m^2/g$ by virtue of equilibrium transport relation (52), and $\Gamma_{b1,2}$ is the vertical face of a possible jump in the bed profile $z_b(x)$. The equations resemble the shock relations of classical shallow-water theory. Equations (57) and (58) express conservation of mass across the jump, and (59) the corresponding momentum balance.

In (59), the integral term represents the horizontal thrust due to the hydrostatic pressure exerted along $\Gamma_{b1,2}$. Since the relevant depth is undefined there (Zanré & Needham 1994), an additional assumption must be made to specify the thrust magnitude. In the limiting case of infinitesimal jumps, the term must reduce to its counterpart $g(h_m + rh_s)(\partial z_b/\partial x)\mathrm{d}x$ in divergence equation (51). This can be achieved by adopting form

$$\int_{\Gamma_{b1,2}} g(h_m + rh_s)\mathrm{d}z_b = g(\langle h_m\rangle_1^2 + r\langle h_s\rangle_1^2)[z_b]_1^2, \tag{60}$$

where the brackets $\langle f\rangle_1^2$ denote a suitably chosen average of the left-hand and right-hand values. This average must be such that hydrostatic balance is strictly satisfied by left-hand and right-hand states for which $z_{b1} \neq z_{b2}$, but $z_{w_1} = z_{w2}$ and $z_{s1} = z_{s2}$ (i.e. a bed discontinuity underlying continuous free surfaces). It can be verified that such is the case for the simple arithmetic mean

$$\langle f\rangle_1^2 = \tfrac{1}{2}(f_1 + f_2). \tag{61}$$

Equation (59) can therefore be rewritten

$$v_\beta = \frac{[(h_m + rh_s)u_m^2 + \tfrac{1}{2}gh_m^2 + \tfrac{1}{2}rgh_s^2]_1^2 + g\langle h_m + rh_s\rangle_1^2[z_b]_1^2}{[(h_m + rh_s)u_m]_1^2}. \tag{62}$$

The Rankine–Hugoniot relations govern the propagation of shocks within the domain. If the flow states to the left and right are uniform and compatible with (57), (58) and (62), then they can be connected by a sharp jump discontinuity propagating at constant speed v_β. To represent stable solutions and have physical meaning, however, such shocks must comply with an additional constraint addressed further in §4.2.

3.4. *Range of validity of the approximation*

The time window in which (49)–(52) and (57)–(59) apply must first be examined. We need, in particular, to verify that the postulated time range does indeed exist. Criterion (53) implies a ratio of geomorphic to frictional time scales such that

$$\frac{t_g}{t_f} \ll 1. \tag{63}$$

From (46) and (48), we have

$$\frac{t_g}{t_f} = \frac{(1 + r)gh_s}{gh_m + rgh_s + 2(1 + r)\mu u_m^2}. \tag{64}$$

In general, alluvial hydraulic studies are concerned with cases where $h_s \ll h_m$, evolving over a time scale of the order of t_f. For bedload conditions (the reasoning above is restricted to contact-load transport), (64) then shows that it is undoubtedly justified to assume instantaneous equilibration of the transport rate. A corollary is that the inner and outer shear stresses become indistinguishable. This is consistent with accepted practice in shallow-water modelling of bedload transport (Armanini & Di Silvio 1988) which considers equilibrium transport and a single bed shear stress function.

For conditions of intense transport in sheet and debris flow modes (where $h_s \sim h_m$), however, the separation of scales is not guaranteed. Further examination is thus required on a case by case basis. For the erosional dam-break waves examined in the present work, the experiments of Capart & Young (1998; see also the analysis and further experiments presented hereinafter), indicate the following sediment transport pattern along the wave; weak transport in sheet-flow mode is observed upstream (hence $h_s \ll h_m$), while the downstream wavefront takes the form of a fully developed debris surge (for which $h_s \approx h_m$). It is for this debris surge that separation of scales t_g and t_f must now be verified.

We will (i) assume separation of scales to hold during the formative stage of this debris surge, then (ii) verify whether or not the resulting effective relaxation times are consistent with the assumption. Accordingly, let a certain time t^* be such that $t^* \gg t_g$, yet $t^* \ll t_f$. This means that erosion has had time to develop fully (and decelerate the flow in the process), but friction due to the residual stress has not yet dissipated much of the flow momentum. We do not know yet if such a time exists. To find out, we want to evaluate the relaxation times effective over the course of the surge development between $t = 0$ and this hypothetical time $t = t^*$. The analysis is not entirely straightforward because relaxation times t_g and t_f do not remain constant during the process. We can obtain effective relaxation times, however, by looking at a suitably chosen collocation point in between the two states of interest.

Since $t^* \gg t_g$, at time t^* the flow has been able to equilibrate its load to its equilibrium transport capacity (i.e. drive the stress difference to zero), hence

$$h_m^* = \mu \frac{u_m^{*2}}{g}, \tag{65}$$

where we have assumed $h_s^* = h_m^*$ corresponding to fully developed, mature debris conditions. Effective relaxation times t_g^{eff} and t_f^{eff} can now be estimated by evaluating (46) and (48) at the intermediate state characterized by a load h_m^{**} midway between initial load $h_m = 0$ and asymptotic load $h_m = h_m^*$, i.e.

$$h_m^{**} = \tfrac{1}{2}(0 + h_m^*). \tag{66}$$

The initial impulse provided by the dam-break discontinuity in water profile has endowed the developing surge with a certain momentum density $q_m^{(0)}$. Over a time range $t \ll t_f$, the residual friction cannot decrease the surge momentum significantly, hence

$$q_m^* \approx q_m^{**} \approx q_m^{(0)}, \tag{67}$$

where $q_m = (1 + r)h_m u_m$ in mature debris conditions. From (65)–(67), we obtain

$$u_m^{**} \approx 2u_m^*. \tag{68}$$

We can now evaluate

$$\frac{t_g^{eff}}{t_f^{eff}} = \frac{t_g^{**}}{t_f^{**}} \approx \frac{gh_m^{**}}{gh_m^{**} + 2\mu u_m^{**2}} \approx \frac{\tfrac{1}{2}\mu u_m^{*2}}{\tfrac{1}{2}\mu u_m^{*2} + 8\mu u_m^{*2}} \approx \frac{1}{20}. \tag{69}$$

There is thus more than an order of magnitude difference between the time scale t_g^{eff}, over which the geomorphic action of the shear stress difference shapes the debris surge, and the time scale t_f^{eff} over which residual friction affects the flow momentum. This result, furthermore, constitutes the worst-case scenario, with a wider separation

applying in the zones of more dilute transport. A further note of interest is that the result is independent of flow and material parameters such as initial depth or sediment density.

The conclusion of the analysis is that, for erosional dam-break waves described by geomorphic shallow-water equations (28)–(29), there always exists a certain time window,

$$t_g < t < t_f, \tag{70}$$

over which, at least in an approximate sense, it is legitimate to assume: (i) instantaneous equilibration of the sediment load h_s; (ii) negligible momentum loss due to residual shear stress τ_{bn} acting on the solid-like side of the bed interface. Note that this double assumption does not neglect all shear stresses; it fully retains the decelerating effect of shear stress difference $\tau_m - \tau_{bn}$, expressed through bulking of the flow with bed material initially at rest. It also retains the accompanying loss of mechanical energy, which constitutes the dominant dissipative effect over the initial stages of the erosional wave development.

Let us now look at where this time window lies with respect to the hydrodynamic time scale t_0. To do so, it is convenient to normalize variables with respect to length h_0 and velocity $(gh_0)^{1/2}$ which characterize the flow hydrodynamics under Froude similarity, i.e.

$$\hat{h}_m = \frac{h_m}{h_0}, \quad \hat{h}_s = \frac{h_s}{h_0}, \quad \hat{u}_m = \frac{u_m}{(gh_0)^{1/2}}. \tag{71a-c}$$

In terms of these non-dimensional variables, the geomorphic time scale t_g is given by

$$t_g = \frac{1}{r \tan \varphi} \left\{ \frac{(\hat{h}_m + r\hat{h}_s)(1 + r)|\hat{u}_m|}{\hat{h}_m + r\hat{h}_s + 2(1 + r)\mu\hat{u}_m^2} \right\} t_0. \tag{72}$$

The product within the curly brackets is of order unity and so is friction factor $\tan \varphi$, hence the ratio of geomorphic to hydrodynamic time scales is of the order of

$$\frac{t_g}{t_0} \sim \frac{1}{r} \sim \frac{1}{s-1} = \frac{\rho_w}{\rho_s - \rho_w}. \tag{73}$$

Two separate cases arise. For natural sediment materials of specific density $s \approx 2.65$, the ratio (73) is of order unity and the geomorphic and hydrodynamic time scales match each other, i.e. $t_0 \sim t_g$. Within a shallow-water description where it is already assumed that $t_0 \ll t$, it is therefore legitimate to assume instantaneous equilibration of sediment load. For the very light sediment materials used in certain laboratory studies, however, the specific density s can be close to one. In that case, it is possible to have

$$\frac{t_g}{t_0} \gg 1, \tag{74}$$

and we must look at times longer than the hydrodynamic time scale to be able to neglect sediment transport relaxation effects. For the dam-break experiments of Capart & Young (1998), for instance, artificial pearls of specific density $s \approx 1.05$ were used, for which

$$\frac{t_g}{t_0} \sim 20. \tag{75}$$

For such conditions, the shallow-water approximation becomes valid faster than the assumption of instantaneous transport equilibration, and a non-equilibrium treatment (as adopted in the computational simulations of Capart & Young) must be adopted

to describe the initial stages of the flow. In the present analytical work, we focus our attention on the window

$$t_g \ll t \ll t_f, \tag{76}$$

corresponding to an intermediate stage of development of erosional dam-break waves, expected to occur earlier for dense sediment material than for light sediment analogues.

4. Riemann solutions

4.1. *System eigenstructure*

Consider the reduced equations in divergence form (49)–(52). Under equilibrium transport constraint (52), they can be transformed by linear combinations into

$$\frac{\partial h_w}{\partial t} + u_m \frac{\partial h_w}{\partial x} + h_w \frac{\partial u_m}{\partial x} = 0, \tag{77}$$

$$\frac{\partial z_s}{\partial t} + 3h_s \frac{\partial u_m}{\partial x} = 0, \tag{78}$$

$$\frac{\partial u_m}{\partial t} + \frac{h_w + h_s}{h_w + 3(1+r)h_s} g \frac{\partial h_w}{\partial x} + \frac{h_w + (1+r)h_s}{h_w + 3(1+r)h_s} g \frac{\partial z_s}{\partial x} + \frac{h_w + 4(1+r)h_s}{h_w + 3(1+r)h_s} u_m \frac{\partial u_m}{\partial x} = 0, \tag{79}$$

where $h_w = z_w - z_s$ is the depth of the water sublayer, $z_s = z_b + h_s$ is the elevation of the top of the sediment transport layer and $h_s = h_s^{eq} = \mu u_m^2 / g$ is the thickness of the latter. System (77)–(79) represents one of various equivalent ways in which the divergence equations can be reduced to a set of three evolution equations for three unknowns, coupled together only through the spatial gradient terms. Equation (77) constitutes a continuity equation for the sediment-free water sublayer. Relation (78) is an Exner equation expressing conservation of the total sediment volume. Finally, (79) is an equation of motion for the heterogeneous flowing mixture.

In the present work, we consider initial conditions for which all the sediment material is saturated with water, i.e.

$$h_w(x, t = 0) \geqslant 0. \tag{80}$$

Furthermore, our phenomenological assumptions do not permit any seepage between the water and sediment phases, precluding any subsequent de-saturation of the granular material. Both the water depth and transport-layer thickness are thus constrained to be positive quantities

$$h_w(x, t) \geqslant 0, \quad h_s(x, t) \geqslant 0. \tag{81a,b}$$

From transport relation (52) and the definitions of the various depths, we obtain

$$\frac{h_w}{h_w + h_s} = \frac{h_m - h_s}{h_m} = 1 - \mu \frac{u_m^2}{gh_m} = 1 - \mu Fr^2, \tag{82}$$

in which $Fr = u_m / (gh_m)^{1/2}$ is the Froude number. Hence, for (82) to comply with constraints (81a) and (81b), we must have

$$-Fr_{max} \leqslant Fr \leqslant Fr_{max}, \tag{83}$$

where $Fr_{max} = 1/\sqrt{\mu}$. The present description therefore implies a limit on the Froude numbers which can be attained physically by the geomorphic flow. The interesting device used by the dam-break wave to comply with this constraint will be discussed

in §4.2. At this stage, condition (83) limits the Froude number interval over which we are to examine the behaviour of (77)–(79).

The coefficients in (78) and (79) depend on the form chosen for constitutive transport relation (52), hampering further physical interpretation. As the explicit algebraic terms bring little insight, from now on we will deal mostly with (77)–(79) in the abstract vector form:

$$\frac{\partial W}{\partial t} + B(W)\frac{\partial W}{\partial x} = 0, \tag{84}$$

where

$$W = \begin{pmatrix} h_w \\ z_s \\ u_m \end{pmatrix},$$

$$B(W) = \begin{pmatrix} u_m & 0 & h_w \\ 0 & 0 & 3h_s \\ \dfrac{g(h_w + h_s)}{h_w + 3(1 + r)h_s} & \dfrac{g(h_w + (1 + r)h_s)}{h_w + 3(1 + r)h_s} & \dfrac{h_w + 4(1 + r)h_s}{h_w + 3(1 + r)h_s}u_m \end{pmatrix}, \tag{85a, b}$$

in which again $h_s = h_s^{eq} = \mu u_m^2/g$.

System (84) forms a set of quasi-linear, first-order partial differential equations. The solution behaviour is controlled largely by the eigenstructure of matrix B. Eigenvalues λ_i are the roots of the third-order polynomial resulting from

$$\det(B - \lambda_i I) = 0, \tag{86}$$

where I is the identity matrix. A complete basis of right eigenvectors $K^{(i)}$ is obtained from the solutions to

$$BK^{(i)} = \lambda_i K^{(i)}. \tag{87}$$

Both the λ_i and $K^{(i)}$ vary with the local flow state W. They can be obtained either algebraically or numerically from (86)–(87). Variable z_s does not intervene in Jacobian matrix B, leaving only u_m and $h_w = h_m - h_s = h_m - \mu u_m^2/g$ as controlling variables for the system eigenstructure. Owing to Froude similarity, the eigenvalues λ_i can then be obtained in normalized form as

$$\frac{\lambda_i}{\sqrt{gh_m}} = f_i(Fr, s), \tag{88}$$

where Froude number $Fr = u_m/(gh_m)^{1/2}$ suffices to characterize the local flow state. The eigenvalues reduce to simple expressions in two limiting cases. For $Fr = 0$, $u_m = 0$ and

$$\lambda_1 = -\sqrt{gh_m}, \quad \lambda_2 = 0, \quad \lambda_3 = \sqrt{gh_m}, \tag{89a–c}$$

hence characteristics λ_1 and λ_3 coincide with their purely hydrodynamic counterparts. For $Fr = \pm Fr_{max}$, on the other hand, $h_w = 0$ and we have

$$\lambda_1 = \left(\tfrac{2}{3} \mp \sqrt{\tfrac{4}{9} + \mu}\right) u_m, \quad \lambda_2 = u_m, \quad \lambda_3 = \left(\tfrac{2}{3} \pm \sqrt{\tfrac{4}{9} + \mu}\right) u_m, \tag{90a–c}$$

thus λ_2 is a purely convective speed. In between these limiting values, the algebraic expressions are cumbersome and it is found more convenient to proceed numerically. The results of such computations are shown graphically in figure 5 for different values of density ratio $s = \rho_s/\rho_w = 1.05, 1.15, 1.5$ and 2.65. From (54), the corresponding
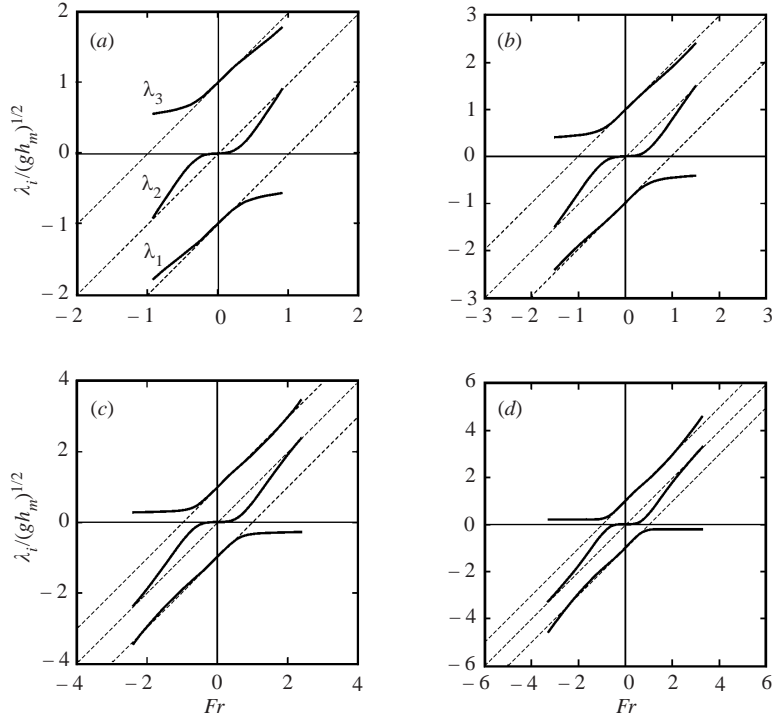
FIGURE 5. Variation of the characteristic wave speeds λ_1, λ_2 and λ_3 with the local Froude number $Fr = u_m/(gh_m)^{1/2}$ for materials of different density ratios $s = \rho_s/\rho_w$, (a) $s = 1.05$; (b) 1.15; (c) 1.5; (d) 2.65. Wave speeds $\lambda_\pm = u_m \pm (gh_m)^{1/2}$ and $\lambda_0 = u_m$ corresponding, respectively, to pure hydrodynamics and passive advection are plotted for reference in dashed lines.

values of the mobility coefficient are $\mu = 1.18$, 0.43, 0.17 and 0.09. The curves illustrate various important properties of the system eigenstructure. First, the eigenvalues are all real and distinct. They can therefore be interpreted as wave speeds and assigned an ordering

$$\lambda_1 < \lambda_2 < \lambda_3, \tag{91}$$

making the system strictly hyperbolic. Wave speeds for positive and negative Froude numbers are antisymmetric, as could be expected on physical grounds. Two of the eigenvalues have the same sign as flow velocity u_m, the last one having opposite sign, a feature encountered also for the equations of alluvial hydraulics (Lai 1991; Morris & Williams 1996). Going from light to heavy sediment material, the characteristic celerities λ_i become closer to those of pure water hydrodynamics $\lambda_\pm = u_m \pm (gh_m)^{1/2}$ (shown in dashed lines in figure 5) but never fully coincide with them.

4.2. Riemann problem and wave structure

As sketched in §1 (see figure 1), the following simple flow configuration is considered in the present work. At time $t = 0$, two constant states W_L and W_R extend infinitely upstream and downstream of an idealized dam:

$$W(x, t = 0) = \begin{cases} W_L & \text{if } x < 0, \\ W_R & \text{if } x > 0, \end{cases} \tag{92}$$

where

$$W_L = \begin{pmatrix} h_w \\ z_s \\ u_m \end{pmatrix} = \begin{pmatrix} h_0 \\ 0 \\ 0 \end{pmatrix}, \quad W_R = \begin{pmatrix} h_w \\ z_s \\ u_m \end{pmatrix} = \begin{pmatrix} 0 \\ 0 \\ 0 \end{pmatrix}. \tag{93}$$

On both sides, a motionless horizontal bed of water-saturated sediments reaches the constant level $z_b = z_s = 0$. Quiescent water of constant depth $h_w = h_0$ is retained upstream, while the water depth is zero downstream. This is a pure initial-value problem for which no boundary conditions are required. Flows governed by homogeneous systems of hyperbolic equations and subject to initial conditions of this type belong to the general class of Riemann problems. Solutions can be constructed in a systematic way (Lax 1957; Jeffrey 1976; Toro 1989), and feature self-similar profiles

$$W(x, t) = W(\xi) = W(x/t), \tag{94}$$

in coordinate $\xi = x/t$ dilating at a constant rate. The profiles result from the composition of three different types of elementary solutions: constant states, centred simple waves, and shock waves. For an $N \times N$ system of equations, there are $N + 1$ constant states (including the two prescribed outer states W_L and W_R) interleaved with N waves, each associated with one of the eigenvalues λ_i of the system. For genuinely nonlinear characteristic fields, these waves are either rarefaction or compression waves.

A rarefaction wave (or 'negative wave' in the terminology of hydraulics) connects two constant states W_l and W_r by a smooth simple wave governed by coupled equations

$$\xi = \frac{x}{t} = \lambda_i, \tag{95a}$$

$$\frac{\mathrm{d}W_i}{K_1^{(i)}} = \frac{\mathrm{d}W_2}{K_2^{(i)}} = \frac{\mathrm{d}W_3}{K_3^{(i)}}. \tag{95b}$$

In the (x, t)-plane, the corresponding flow states $W(\xi)$ remain constant along straight rays (95a), radiating from the origin at an inclination $\mathrm{d}x/\mathrm{d}t = \lambda_i$ given by characteristic celerity $\lambda_i(W)$. Within the fan-like region, the wave shape is then determined by condition (95b) involving variations in the flow variables W_j normalized by their respective components $K_j^{(i)}$ in eigenvector $K^{(i)}$. These ratios are the generalized Riemann invariants of the ith simple wave (Jeffrey 1976; Toro 1989). In special cases (such as the classical shallow-water equations), the coupled ODEs (95b) can be integrated explicitly and yield actual invariants. In general, however, numerical quadrature must be used. For a rarefaction wave to form, divergence of the associated characteristic wave speed $\lambda_i(W)$ must be observed from one side of the fan to the other, i.e.

$$\lambda_i(W_l) < \lambda_i(W_r). \tag{96}$$

The simple wave profiles are connected to the left and right constant states W_l and W_r by discontinuities in the first derivatives, called weak shocks or 'creases'. These constitute legitimate features as they propagate along characteristic curves $\mathrm{d}x/\mathrm{d}t = \lambda_i(W_l)$ and $\mathrm{d}x/\mathrm{d}t = \lambda_i(W_r)$, which are potential carriers of weak discontinuities.

A compression wave (or 'positive' wave), on the other hand, connects two constant states W_l and W_r by a single jump discontinuity, or strong shock, subject to Rankine–Hugoniot equations of the type (57)–(59). For such a shock to arise and remain stable, left and right constant states must further satisfy the so-called 'entropy condition':

$$\lambda_i(W_l) > v_i > \lambda_i(W_r), \tag{97}$$

where v_i is the speed of the shock and λ_i the eigenvalue associated with the ith elementary wave. Geometrically, condition (97) requires that characteristics of the same family converge onto the path traced by the shock in the (x, t)-plane. For given initial conditions and hyperbolic equations, the construction of a complete profile thus requires the identification of a suitable wave structure, i.e. the selection of a set of elementary waves satisfying either (96) or (97). Under certain mathematical restrictions, it can then be proved (Lax 1957) that the composite solution to the Riemann problem is unique and stable.

This general theoretical background can now be applied to the problem at hand. Reduced system (84) is a 3×3 homogeneous hyperbolic system, and we are to identify a wave structure composed of 4 constant states and 3 elementary waves of the rarefaction or compression variety, compatible with either (96) or (97). The two outer constant states W_L and W_R are prescribed, leaving two inner states W_L^* and W_R^* which are unknown and part of the solution. Selection of the 3 elementary waves is based on the following reasoning. By analogy with the Ritter solution (Ritter 1982; Stoker 1957), the upstream wave associated with eigenvalue λ_1 is expected to be a rarefaction wave. With reference to figure 5, for $Fr > 0$ we have $\lambda_1 < 0$ throughout, and it is the only negative wave speed. The associated rarefaction fan is therefore entirely contained in the negative half $x < 0$ of the (x, t)-plane. Yet, when sediment mobility μ tends to zero, solutions of the geomorphic problem must approach the rigid-bed solutions. Since the single rarefaction wave of the Ritter solution spans both the upstream and downstream regions, it is anticipated that a second rarefaction wave, entirely contained in the positive half $x > 0$ of the (x, t)-plane will be associated with λ_2. In the limiting case of zero mobility, the two rarefactions of the erosional wave can thus merge into the single rarefaction of the Ritter solution.

The third elementary wave is of a different kind. In the rigid-bed case, the Riemann problem with zero water depth downstream of the dam yields a free surface profile which decreases smoothly to zero at the forefront (Ritter 1892; Dressler 1954). Under the present assumptions, this does not carry over to the erodible bed case. To see why, recall that our equilibrium transport assumption implies

$$\frac{h_s}{h_m} = \frac{h_s^{eq}}{h_m} = \frac{\mu u_m^2}{g h_m} = \mu Fr^2. \tag{98}$$

For a wave tip going continuously to zero depth while propagating at a finite speed u_m, this would imply $h_s/h_m \to \infty$. By definition, $h_m = h_s + h_w$, and this would in turn force a negative water depth. Such an outcome would require de-saturation of the granular material, an outcome forbidden by the present description as we assume no seepage between the water and granular phases. This leaves only the alternative solution, which is the formation of a discontinuous shock overrunning the saturated granular bed. The downstream side of the wave is the undisturbed right state W_R of the erosional Riemann problem, for which $h_{wR} = 0$, $h_{sR} = 0$ and $z_{bR} = 0$. To the left is the yet unknown inner right state W_R^*. Applied to this configuration, the Rankine–Hugoniot equations (57) and (58) expressing conservation of mass for the water and sediment phases become

$$v_S = \frac{h_{mR}^* u_{mR}^*}{z_{bR}^* + h_{mR}^*}, \tag{99}$$

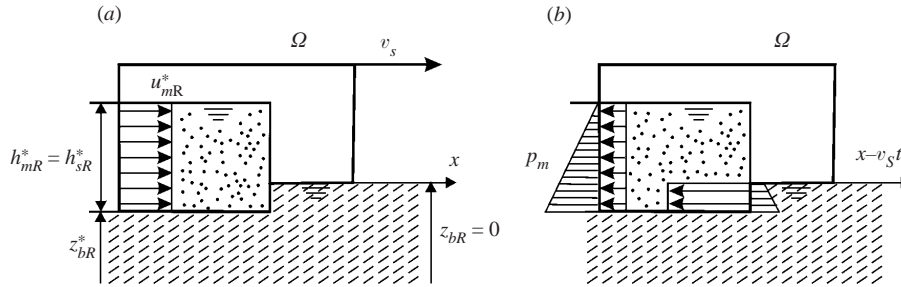$$v_S = \frac{h_{sR}^* u_{mR}^*}{z_{bR}^* + h_{sR}^*}, \tag{100}$$

(a)

(b)

FIGURE 6. Erosional bore at the head of the wave. The fully developed debris snout advances into an undisturbed region where the saturated granular material is at rest, (a) shock configuration; (b) control volume and components of the momentum balance as seen in a frame of reference travelling with the bore.

where v_S is the shock speed. The only way of simultaneously satisfying (99) and (100) for non-zero u_{mR}^* is to let $h_{mR}^* = h_{sR}^*$. State W_R^* thus corresponds to fully developed debris flow conditions, for which the transport layer invades the entire flow depth. To overrun a saturated granular bed with no overlying depth of pure water, the only kinematically allowable wave (in the absence of slip or seepage) is a debris surge having the same water–sediment composition as the original loose bed. Under equilibrium transport constraint (52), identity $h_{mR}^* = h_{sR}^*$ further implies

$$Fr_R^* = \frac{u_{mR}^*}{\sqrt{g h_{mR}^*}} = \frac{1}{\sqrt{\mu}} = Fr_{max}. \tag{101}$$

Hence, state W_R^* immediately upstream of the shock has its Froude number determined entirely by the sediment mobility μ. The shock is precisely the device required by the erosional dam-break flow if it is to comply with the bound $Fr \leqslant Fr_{max}$ identified earlier.

Finally, the dynamic balance of the shock is governed by Rankine–Hugoniot momentum equation (62). For the conditions outlined above and letting $h_{mR}^* = h_{sR}^*$, the relation reduces to

$$v_S = \frac{h_{mR}^* u_{mR}^{*2} + \frac{1}{2} g h_{mR}^* (h_{mR}^* + z_{bR}^*)}{h_{mR}^* u_{mR}^*}. \tag{102}$$

The general features of the shock as well as the terms involved in its momentum balance are illustrated in figure 6. A positive step-like surge in the flow free surface is mirrored by a negative step in the bed profile. As this erosional front progresses along with the shock, an initially static layer of water and sediment is set in motion and engulfed into the flowing mixture. Note that the step in bed profile results from the wave development: the initial conditions (figure 1) do not involve any bed indentation. The erosional bore is driven by the hydrostatic pressure thrust applied over its upstream depth, lowered by a smaller opposite pressure thrust expressed on the vertical face of the step in bed profile. The main resisting effect comes from bulking of the surge with eroded material, continuously feeding inertia that the flow must accelerate. The shock speed is such that this inertia flux balances exactly the pressure thrust. We propose to use the term 'erosional bore' to refer to this special shock.

Piecing together the four constant states, the two rarefaction waves and the erosional bore, we obtain the wave structure and composite profiles shown on figure 7. On the basis of that blueprint, we can proceed with the step-by-step construction of solutions
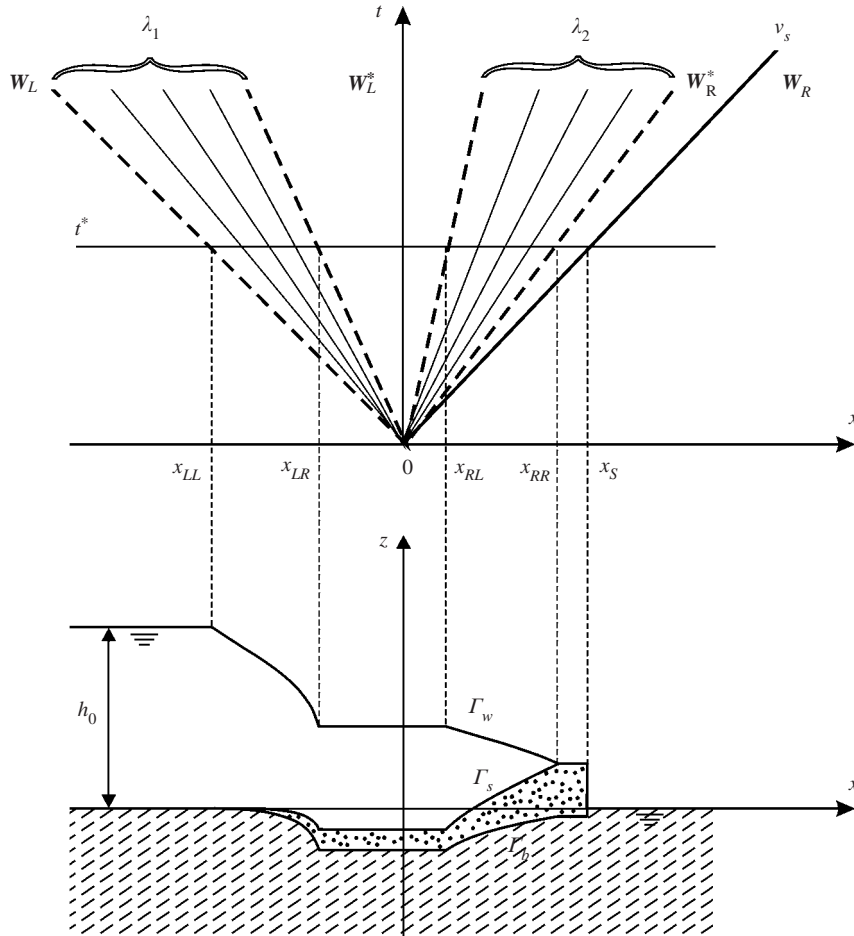
FIGURE 7. Wave structure of the erosional dam-break flow. Top: characteristic fans and shock path. Bottom: flow pattern as depicted by the three interface profiles Γ_w, Γ_s and Γ_b.

in §4.3. The postulated wave structure will be validated *a posteriori* by verifying that the compatibility equations (96) or (97) do indeed hold for the obtained waves.

4.3. *Integration procedure and results*

Detailed wave profiles are constructed by traversing the wave structure from one end to the other at a given time instant. We will progress from upstream to downstream (left to right) along the transect $t = t^* = \mathrm{const}$ shown in figure 7. Along this transect, intersections with the boundaries of the different wave regions are encountered at the following locations: x_{LL} is the upstream edge of the wave, where the left constant state W_L is reached at time t^* by the upstream rarefaction associated with a fan of λ_1 characteristics; x_{LR} is the point at which this rarefaction wave meets the upstream inner constant state W_L^*; x_{RL} is the downstream limit of this constant state, where it gives way to the second rarefaction wave associated with a fan of λ_2 characteristics; x_{RR} is the downstream edge of the second rarefaction, where it meets the downstream constant state W_R^*; finally, x_S is the position of the shock-like erosional bore connecting the downstream inner constant state W_R^* to the undisturbed right constant state W_R. The locations of these various feature-points are unknown

and must form part of the solution. The inner constant states W_L^* and W_R^* are also unknown. To proceed with the integration, we must make an initial guess for one of the components of the upstream inner constant state, say the velocity u_{mL}^*.

Having made that initial guess, let us advance along the transect starting from the left constant state W_L. Equations (95a,b) can first be applied to the upstream rarefaction wave. Its leftmost edge has celerity $\lambda_{LL} = \lambda_1(W_L)$ where $W_L = (h_0\ 0\ 0)^T$ is known, hence by virtue of (95a) we have

$$x_{LL} = \lambda_{LL} t^* = -(gh_0)^{1/2} t^*, \tag{103}$$

where we have used the simple expression (89a) for wave speed λ_1 in the case $Fr = 0$. The upstream edge of the erosional dam-break wave coincides with the upstream edge of the Ritter and Stoker solutions for dam-break flow over a rigid bed. Advancing into the rarefaction, the smoothly varying profile of the simple wave is obtained by integrating the generalized Riemann invariants (95b) associated with the first family of eigenvalues λ_1:

$$\frac{dh_w}{K_1^{(1)}(W)} = \frac{dz_s}{K_2^{(1)}(W)} = \frac{du_m}{K_3^{(1)}(W)}, \tag{104}$$

complemented by (95a)

$$\frac{x}{t^*} = \lambda_1(W) = f_1(Fr, s)\sqrt{gh_m} = f_1\left(\frac{u_m}{\sqrt{gh_m}}, s\right)\sqrt{gh_m}, \tag{105}$$

where it is to be recalled that $W = (h_w\ z_s\ u_m)^T$, $h_m = h_w + \mu u_m^2/g$, $K_j^{(i)}(W) = j$th component of the i-eigenvector of Jacobian matrix B, and $f_i(Fr, s) = i$th normalized wave speed as plotted in figure 5. The integration is easily performed numerically using a second-order Runge–Kutta method. Integration is pursued until $u_m = u_{mL}^*$ and the upstream inner constant state W_L^* is reached. At this stage, the other components h_{wL}^* and z_{sL}^* of W_L^* are known from integration of (104), and the position x_{LR} where the first rarefaction meets the upstream inner constant state is obtained from (105).

Equations (95a,b) can now be applied again to the downstream rarefaction wave associated with speed λ_2. Its leftmost edge has celerity $\lambda_{RL} = \lambda_2(W_L^*)$ where W_L^* is known from the previous step, hence from (95a) we have

$$x_{RL} = \lambda_2(W_L^*)t^*. \tag{106}$$

The profile of the second rarefaction is obtained by integrating the generalized Riemann invariants (95b) associated with the second family of eigenvalues λ_2:

$$\frac{dh_w}{K_1^{(2)}(W)} = \frac{dz_s}{K_2^{(2)}(W)} = \frac{du_m}{K_3^{(2)}(W)}, \tag{107}$$

complemented by (95a)

$$\frac{x}{t^*} = \lambda_2(W). \tag{108}$$

This integration is pursued until erosional bore condition (101) is met, i.e.

$$\frac{u_m}{\sqrt{gh_m}} = Fr_{max} = \frac{1}{\sqrt{\mu}}, \tag{109}$$

or equivalently when position

$$x_{RR} = \lambda_2(W_R^*)t^* = u_m t^* \tag{110}$$

is reached, resorting to expression (90b) for wave speed λ_2 in the case $Fr = Fr_{max}$.

At this point, the second inner constant state W_R^* and its left bound x_{RR} are fully specified as a result of the integration. The position x_S of the shock is further obtained from (99) as

$$x_S = v_S t^* = \frac{h_{mR}^* u_{mR}^*}{z_{bR}^* + h_{mR}^*} t^*, \tag{111}$$

where it is to be recalled that $z_b = z_s - h_s = z_s - \mu u_m^2/g$. A point of interest here is that, as illustrated in figure 6, the flow velocity u_{mR}^* upstream of the shock is smaller than the shock speed, as required if the bore is to erode material from the bed. There remains one shock condition which has not been used: the dynamic balance equation (102), i.e.

$$v_S = \frac{h_{mR}^* u_{mR}^{*2} + \frac{1}{2} g h_{mR}^* (h_{mR}^* + z_{bR}^*)}{h_{mR}^* u_{mR}^*}. \tag{112}$$

This last condition will not be met owing to the arbitrary initial guess made for value u_{mL}^* at the start of the procedure. We must therefore revise estimate u_{mL}^* and repeat the procedure iteratively until condition (112) is satisfied. The solution accuracy can be evaluated by checking conservation of the total material volume. The relative error (with respect to the water volume involved in the wave) was verified to be less than 0.01% for the results presented here. Shooting methods similar to the one described above are used to solve Riemann problems in the related context of gas dynamics (Toro 1989).

Results from the above procedure are presented in figure 8. Profiles of the three interfaces Γ_w, Γ_s and Γ_b specify the solutions completely. They are shown for four different values of density ratio $s = \rho_s/\rho_w = 1.05$, 1.15, 1.5 and 2.65 (identical to the values chosen for the eigenvalue plots of figure 5). The most common conditions encountered in nature (quartz sand in water) correspond to $s = 2.65$ (figure 8d). The other profiles (figure 8a–c) correspond to lighter materials often used as sediment analogues in laboratory studies. The solutions are shown in non-dimensional form as a function of $x/(t(gh_0)^{1/2})$, and remain self-similar in time. Overall, even though the wave structure is more complex, the solutions are reminiscent of the Stoker and Ritter profiles for dam-break flow over a rigid bed. Erosion of the bed material leads to the formation of a scour hole which is deepest in the near-dam region. A negative wave recedes upstream, its leading edge featuring a crease in the free surface Γ_w and a smooth transition in the bed profile Γ_b. Within the first rarefaction region, the water free surface Γ_w and sediment interface Γ_s slope in the same downstream direction. A region of constant state is obtained at the centre of the wave (encompassing the origin where the dam was located), where the water level rises to a height z_w which is slightly higher than would be obtained over a rigid bed ($z_w = \frac{4}{9} h_0$ for the Ritter solution). Downstream, the second rarefaction exhibits opposite gradients in the water free surface Γ_w and sediment interface Γ_s. The two interfaces converge together at the downstream edge of the rarefaction where $z_s = z_w$ and the transport layer occupies the whole depth of the flow. A constant state characterized by mature debris flow conditions extends onwards over a smaller length than the central constant state. Finally, a shock-like erosional bore forms the forefront of the wave, incorporating a thin layer of motionless material as it advances. As manifested by the thickness $h_s = z_s - z_b = \mu u_m^2/g$ of the transport layer, the velocity grows monotonously from upstream to downstream. The corresponding Froude numbers $Fr = u_m/(gh_m)^{1/2}$ go from zero upstream to $Fr = Fr_{max}$ in the debris snout region at the head of the wave.
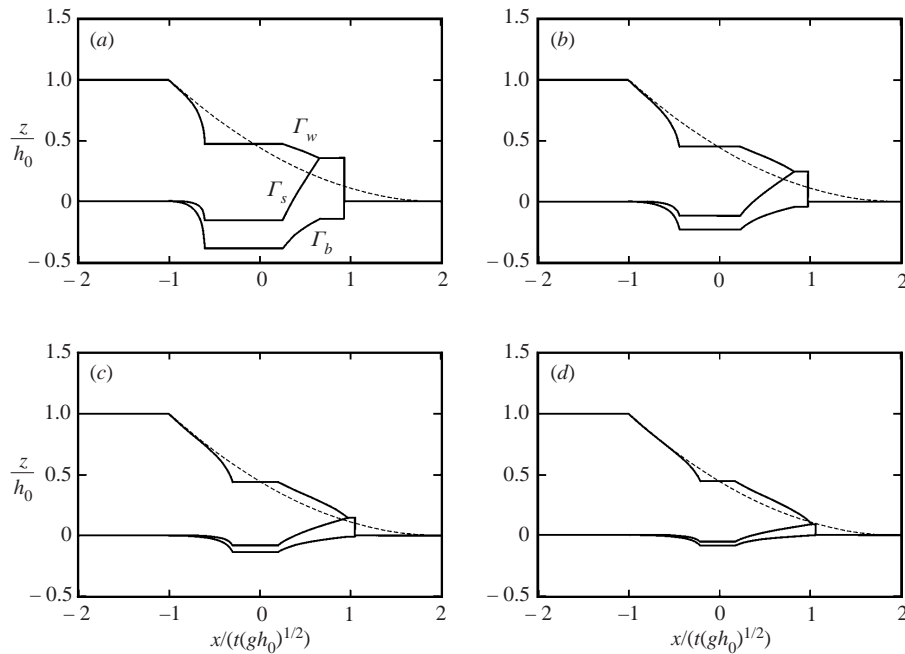
FIGURE 8. Riemann solutions for the erosional dam-break wave, computed for materials of various density ratios $s = \rho_s/\rho_w$, (a) $s = 1.05$; (b) 1.15; (c) 1.5; (d) 2.65. The Ritter solution for dam-break flow over a dry frictionless bottom (dashed line) is also shown for reference.

Although the computed profiles all share these basic qualitative features, contrasting results are obtained for the four different density ratios. Away from the forefront, the profiles come closer to the Ritter solution (shown for reference as a dashed curve) when material density is increased. Features which are most affected by relative density s are the scour depth and the spatial extent of the two inner constant states. For light materials, sediment mobility is high and a thick transport layer is obtained. As a result, erosion reaches deep into the underlying substrate. The central scour hole and the mature debris snout furthermore make up a high proportion of the overall length of the wave. The converse is true for heavier materials. Transported sediment volumes are thus sensitive to the material density.

Other features of the flow profiles are only weakly affected by changes in the density ratio. The celerity of the leading edge of the upstream negative wave does not vary at all with the bed material composition. The water elevation z_{wL}^* of the left inner constant state, in the region encompassing the original dam position, does not evolve much either. Perhaps more surprisingly, the speed of the debris snout is almost independent of the density ratio. The erosional bore propagates into the undisturbed downstream region at a speed of around $v_S \approx (gh_0)^{1/2}$ (close to half of the speed of the Ritter wavefront over a rigid frictionless bed $= 2(gh_0)^{1/2}$) which changes very little with the density of the loose bed material. For dense sediment, it would appear that the layer of eroded material is thinner but also heavier, hence it continues to inject significant inertia into the body of the wave. The Stoker solution for pure water dam-break waves over a rigid bottom also features a very stable shock speed $v_S \approx (gh_0)^{1/2}$ (to within 10%) when the tailwater depth to reservoir depth ranges from $h_R/h_L = 1$ all the way down to $h_R/h_L = 0.05$ (Stoker 1957). Only for very small tailwater depths $h_R < \frac{1}{20}h_L$ does the shock speed vary significantly and start approaching the dry bed
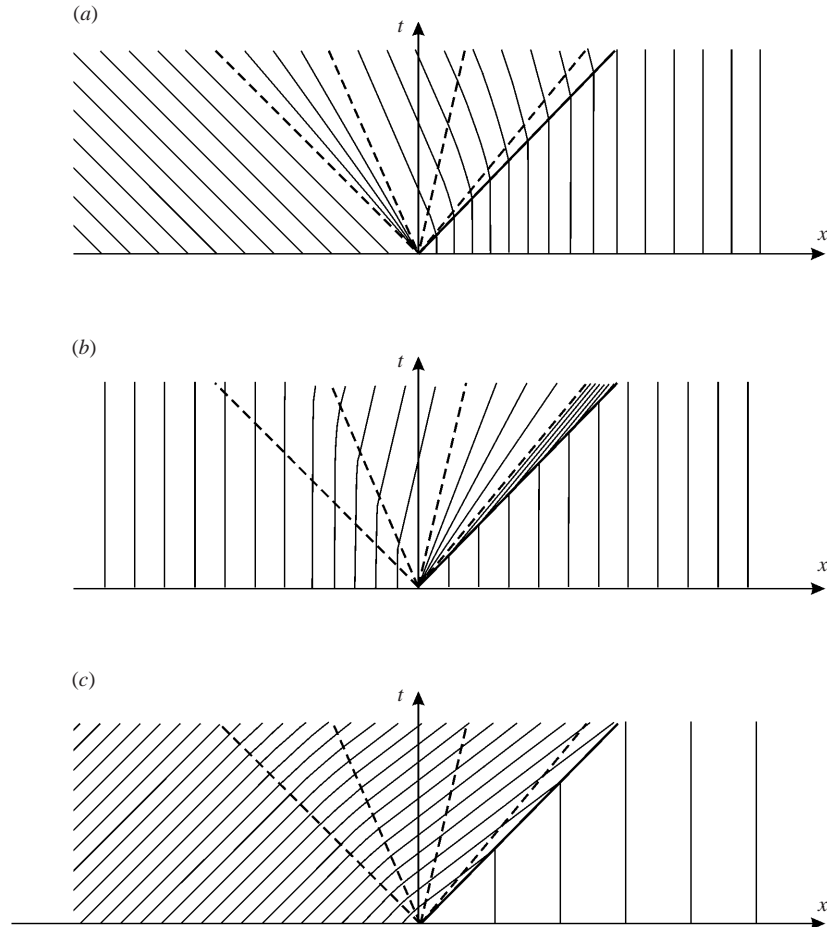
FIGURE 9. Characteristic paths $\Lambda_i = \mathrm{d}x/\mathrm{d}t = \lambda_i$ computed for the case $s = \rho_s/\rho_w = 1.15$, (a) λ_1 family; (b) λ_2 family; (c) λ_3 family. The two simple wave regions feature fans of diverging characteristics belonging to the λ_1 and λ_2 families, respectively. They are bounded by weak shocks (creases) propagating along the characteristics shown in dashed lines. Characteristics of the λ_3 family converge onto the shock path shown as a thick continuous line.

value of $2(gh_0)^{1/2}$. This suggests that a general physical principle might be involved, constraining the approximate shock speed regardless of the specific conditions. We were not able, however, to ascertain what such a principle might be.

In figure 9, characteristic paths Λ_i are plotted in the non-dimensional (x, t)-plane for a wave involving sediment material of relative density $s = 1.15$. They result from the numerical integration in time of ODEs $\mathrm{d}x/\mathrm{d}t = \lambda_i$ associated with each of the three families of eigenvalues λ_i. The curves form parallel rays inside each of the constant state regions. Within the first and second rarefaction regions, respectively, characteristics from the λ_1 and λ_2 families form fans of straight rays radiating from the origin. Condition (96) requiring divergence of characteristics across simple wave regions is thus met. At the wavefront, finally, characteristics of the λ_3 family converge from both sides toward the shock path. This verifies 'entropy' condition (97). Similar patterns are obtained for other values of the density ratio. The anticipated wave structure is therefore validated, and the Riemann profiles represent meaningful solutions to the reduced governing equations.

5. Experiments and comparison of results

5.1. *Experimental apparatus and methods*

The theoretical description derived above can now be compared with two sets of experimental data. Performed in Taipei (National Taiwan University) and Louvain-la-Neuve (Université catholique de Louvain). Both sets concern small-scale laboratory dam-break waves of initial water depth $h_0 = 10$ cm released over erodible beds in prismatic channels. They differ primarily in the sediment material used. For the Taipei tests, reported previously in Capart & Young (1998), a very light sediment analogue was adopted. The grains are artificial pearls covered with a shiny white coating, spherical in shape, having a diameter of 6.1 mm, density $\rho_s = 1048$ kg m^{-3}, and fall velocity $w \approx 7$ cm s^{-1}. The corresponding density ratio $s = \rho_s/\rho_w = 1.048$ makes the material barely heavier than water. For the new tests performed in Louvain-la-Neuve, denser sediments were chosen. These consist of cylindrical PVC pellets having the following characteristics: diameter $= 3.2$ mm; height $= 2.8$ mm (hence an equivalent spherical diameter of 3.5 mm); density $= 1540$ kg m^{-3}; fall velocity $w \approx 18$ cm s^{-1}. The corresponding density ratio is $s = 1.54$. The PVC particles are mostly white, mixed with a small proportion of black grains used for quick motion inspection. As the two sets of experiments involve similar devices and procedures, they are described together in what follows.

The type of apparatus used for both series of tests is shown schematically in figure 10, along with a photograph of the Louvain set-up. Tests are performed in horizontal prismatic flumes of rectangular cross-section. The test reach for the Taipei experiments was of length $= 1.2$ m, width $= 20$ cm and sidewall height $= 70$ cm. For the Louvain tests the dimensions were length $= 2.5$ m, width $= 10$ cm and sidewall height $= 35$ cm. Before each run, the granular material is placed within the test reach and profiled into a layer of constant thickness of approximately 5–6 cm. To represent the idealized dam, a sluice gate fitted with watertight joints is lowered down to the flume bottom at the centre of the test reach. Water is introduced downstream of the gate up to the level of the granular bed, so as to fully saturate the sediments. Upstream, the water level is raised to a depth of $h_0 = 10$ cm above the top of the granular bed. The dam-break wave is then released by rapidly lifting the sluice gate, using either a system of springs (Taipei) or a weight and pulley mechanism (Louvain). In both cases, the gate is verified to clear the water surface within 50 ms.

The resulting flows are filmed through the transparent sidewalls using fast CCD cameras, operating at frame rates of 100 images per second (Taipei) and 200 frames per second (Louvain). The grey level images have a resolution of 256×256 pixels, which is too low to capture at once the full spatial extent of the waves. Tests are therefore repeated a number of times with the camera (or the gate, for the Louvain tests) displaced upstream or downstream. Two synchronized CCD cameras were available in Louvain, doubling the length which could be acquired for each run, but it was still insufficient to obtain the desired coverage. The image sequences resulting from separate runs are later reassembled to form coherent mosaics. Such a procedure is feasible because tests are highly repeatable, as verified by filming separate events in exactly the same configuration. Frontal lighting comes from spot heads oriented at an angle of 45° with respect to the camera axis. To avoid projected shallows, a soft box placed on the other side of the flow provides diffuse back lighting. This yields clear images in which the white sediment grains stand out from the surrounding darker fluid, and the flow free surface contrasts well with the background. Reconstituted image mosaics of the flows are shown in figures 12 and 14 for the Taipei and Louvain
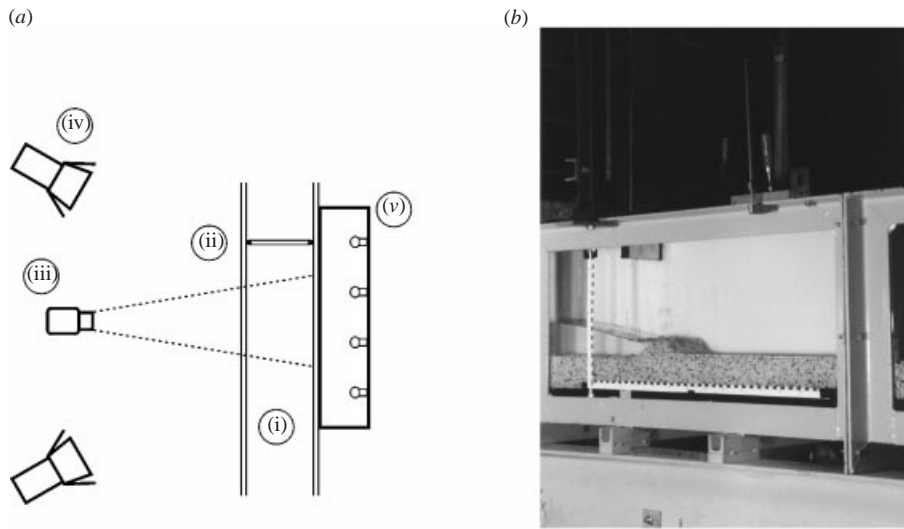
FIGURE 10. Experimental apparatus, (*a*) schematic top view; (*b*) side view of the laboratory set-up in Louvain-la-Neuve moments after release of an erosional dam-break wave (photograph courtesy of J.-L. Van Goethem & L. Villers). The components of the device are: (i) prismatic flume with transparent sidewalls; (ii) sluice gate; (iii) CCD camera; (iv) spot heads; (v) back-illumination soft box.
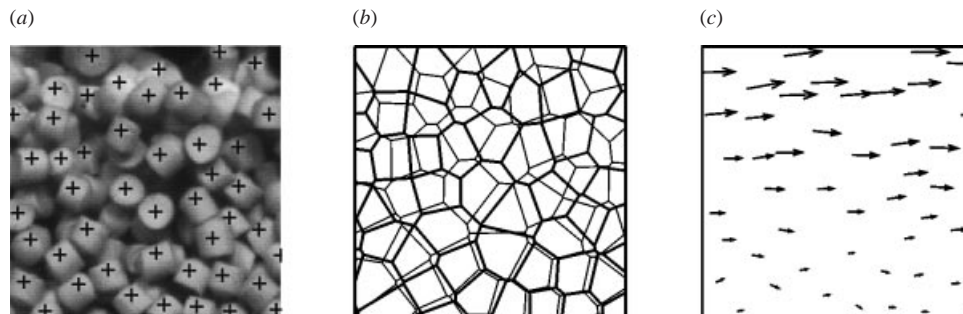

FIGURE 11. Steps of the pattern-based particle tracking velocimetry algorithm (Capart *et al.* 2001); (*a*) image detail with particle centroid positions; (*b*) Voronoï diagrams constructed on the sets of particle centres identified on one frame (thin lines) and the next (thick lines); (*c*) displacement vectors obtained by matching the particles according to their local Voronoï patterns.

tests, respectively. As pressure gradients and inertia effects dominate over friction in the first stages of wave development, the sidewalls are expected to have a negligible influence on the observations. This was verified by filming flows from oblique and vertical angles and checking that the profiles are uniform in the transverse y-direction.

Digital particle tracking velocimetry (DPTV) is used to acquire the individual grain motions and visualize the transport pattern. For the results originally presented in Capart & Young (1998), the tracking was performed using a manually supervised procedure requiring painstaking work. Some of these measurements are reproduced here in figures 13(*b*), 13(*c*) and 13(*e*). In the interval, fully automated algorithms suitable for the imaging of rapid granular flows were developed (Capart *et al.* 2001). The main challenge lies in resolving motion ambiguities in dense rapidly sheared particle dispersions. The pattern-based principle adopted to carry out this task is
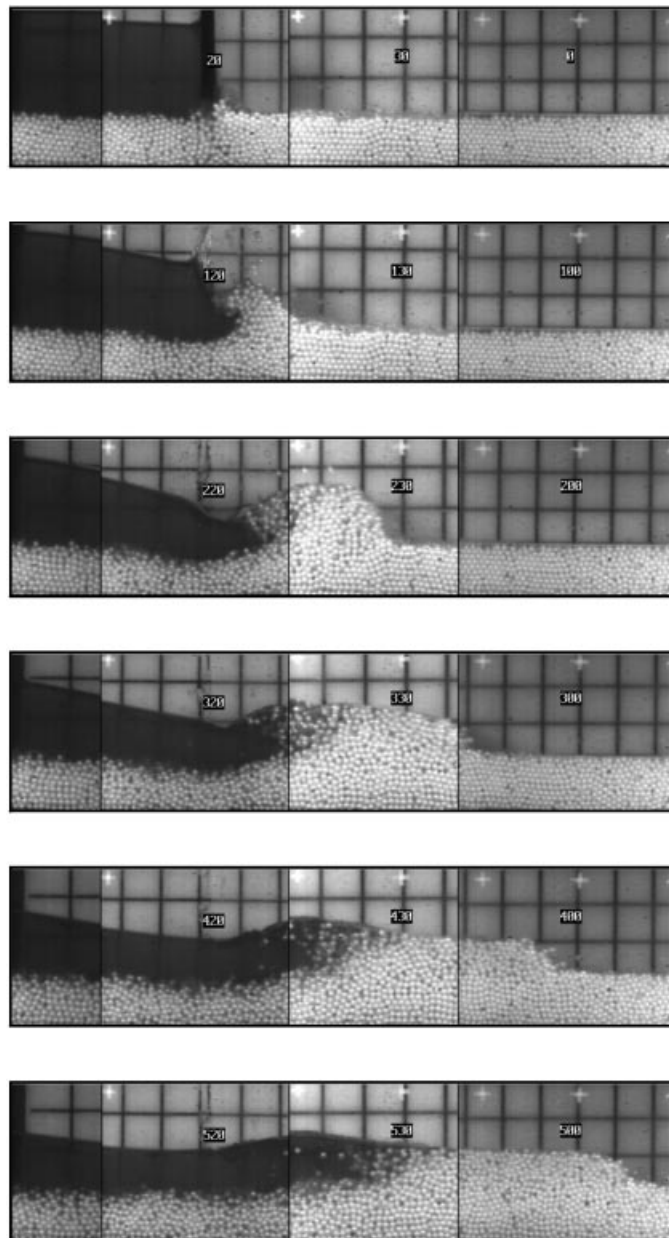
FIGURE 12. Image mosaics for the Taipei erosional dam-break wave experiments, conducted with light granular material ($s = \rho_s/\rho_w = 1.048$). The instants selected are, from top to bottom: $t = 0$; 0.1 s; 0.2 s; 0.3 s; 0.4 s; 0.5 s. Digital footage from the experiments of Capart & Young (1998).

illustrated on figure 11. Convolution of the digital images with radial filters is first used to highlight particles and locate their centroid positions to subpixel accuracy. Voronoï diagrams are then constructed on the sets of particle centres identified on one frame and on the next (shown, respectively, in thin and thick lines). Although the particles themselves are identical, their Voronoï polygons are not and reflect the local arrangement of neighbouring grains. This arrangement turns out to be quite stable over successive frames. By matching polygons of similar shapes, it is possible to pair
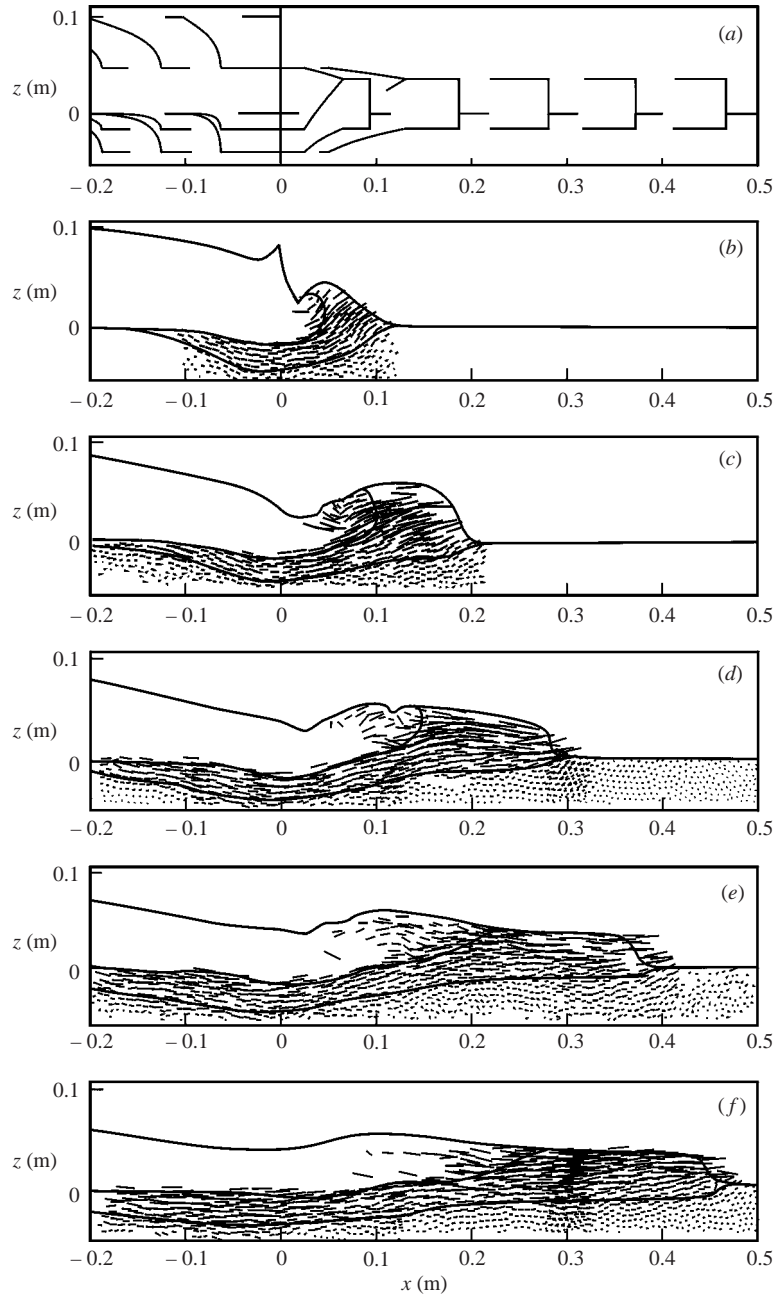
FIGURE 13. Velocity fields and interfaces for the Taipei erosional dam-break wave experiments, (a) silhouettes of the theoretical solution plotted for reference; (b)–(f) particle displacements tracked over 6 successive frames (50 ms) for $t = 0.1$ s, 0.2 s, 0.3 s, 0.4 s, 0.5 s. Estimated interfaces Γ_w, Γ_s and Γ_b superimposed as thick lines.

positions corresponding to one and the same physical particle but sampled at two separate times. Once such a pairing is obtained, the inter-frame displacement vectors of the individual particles approximate the velocity field. Full details of the methods are given in Capart *et al.* (2001).
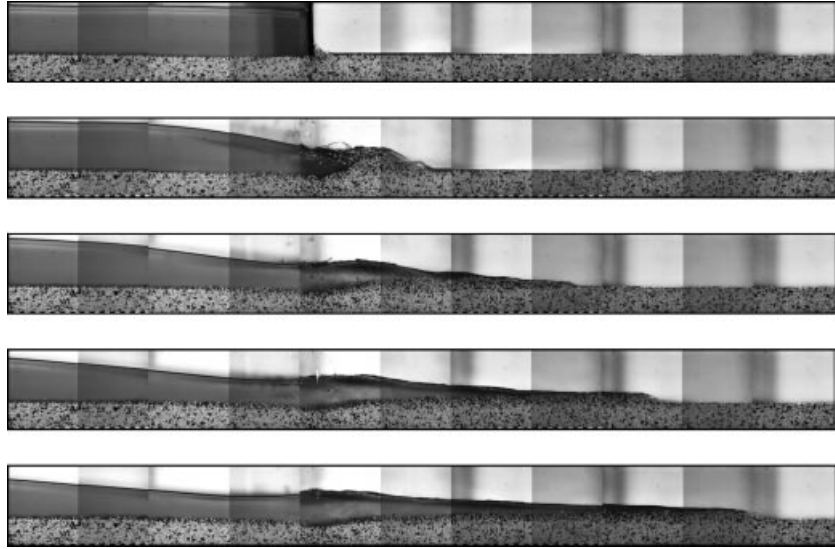
FIGURE 14. Image mosaics for the Louvain erosional dam-break wave experiments, conducted with granular material of intermediate density ($s = \rho_s/\rho_w = 1.54$). The instants selected are, from top to bottom: $t = 0$; 0.25 s; 0.50 s; 0.75 s; 1.00 s. Digital footage courtesy of B. Spinewine, Université catholique de Louvain.

Additional results for the Taipei tests of Capart & Young (1998) obtained using the new algorithms are shown on figures 13(d) and 13(f), where it is seen that they yield results identical in quality to those obtained previously with manually assisted methods. The latter would not have been a practical option for the new series of tests performed in Louvain, as these feature a much larger number of smaller particles. For this series, particle tracking results derived using the fully automated methods are presented in figure 15. The only manual intervention involved in obtaining the new velocity results is a post-processing step in which some manifestly incorrect vectors (around 2% of the total number of vectors) are pruned out.

Experimental profiles for the three interfaces Γ_w, Γ_s and Γ_b introduced above as part of the theoretical description are extracted in the following way. The flow free surface Γ_w separating the water layer or water–granular mixture from the overlying ambient air is obtained by manually tracing the flow silhouette on the digital images shown on figures 12 and 14. Interface Γ_s dividing the flow into sediment-free and sediment-rich regions is acquired in a similar way directly from the digital images. Finally, the location of bed interface Γ_b distinguishing the moving transport layer from the underlying motionless bed is estimated on the basis of the PTV displacement fields. Roughly, the interface position is chosen as the location where a linear extrapolation of the upper velocity profile intercepts zero, leaving a decaying tail of small velocities below the interface. The three boundaries are superimposed onto the displacement fields shown on figures 13 and 15. Some degree of judgement is involved in tracing these various curves, hence they are not to be interpreted too literally. As can be seen from the raw images and displacement fields, however, the interfaces usefully highlight the main aspects of the flow structure.

5.2. *Phenomenological overview*

The Taipei measurements pertain to a time window between $t = 0$ to $t \approx 5t_0$ where $t_0 = (h_0/g)^{t/2}$ is the hydrodynamic time scale. The time cutoff $t \approx 5t_0$ lies at the lower
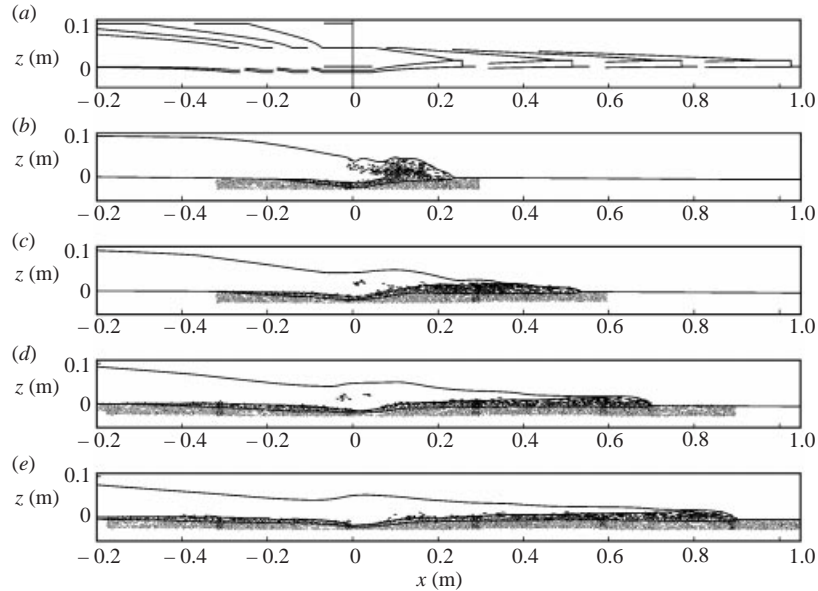
FIGURE 15. Velocity fields and interfaces for the Louvain erosional dam-break wave experiments, (*a*) silhouettes of the theoretical solution plotted for reference; (*b*)–(*e*) particle displacements tracked over 4 successive frames (15 ms) for $t = 0.25$ s, 0.50 s, 0.75 s, and 1.00 s. Estimated interfaces Γ_w, Γ_s and Γ_b superimposed as thick lines.

end of the range $t \gg t_0$ in which the shallow-water assumption is expected to become valid. An even more serious limitation is that, according to the analysis of § 3.3, this time window comes too soon to rule out non-equilibrium sediment transport effects. Because of the very light sediment used ($s \approx 1.05$), the time required for the flow to equilibrate its sediment load is estimated from (73) as $t_g \sim 20t_0$. The Taipei conditions therefore fall outside the range in which our theoretical description rigorously applies. Despite this caveat, the results remain instructive. The high sediment mobility makes the transport process quite salient, more so than for the tests with denser material, illuminating a number of features of the phenomena. For various properties of the wave, the theory also turns out to yield reasonable results. The limitations must nonetheless be borne in mind, and they motivated the new series of experiments conducted in Louvain. A longer coverage is obtained for these tests, which extend from $t = 0$ to $t \approx 10t_0$. Because of the heavier material, furthermore, the equilibrium transport assumption becomes valid sooner, and applies to times greater than $t_g \sim t_0$. This places the Louvain tests in a range which is more consistent with the expected domain of validity of the present theory.

The experimental results presented in figures 12–15 clearly depict the main processes involved. The water surge released by the gate quickly entrains bed sediment in its motion. This bulking of the surge with eroded material is most severe for the light sediment material of the Taipei tests (figures 12 and 14), but is also significant for the heavier material of the Louvain experiments (figures 13 and 15). In both cases, immediate erosion is most intense in the vicinity of the dam, yet scouring progresses both upstream and downstream as the wave develops. These qualitative features match the field observations mentioned in the introduction for the case of the Ha! Ha! lake breakout flood (figure 2). While the short time behaviour in the vicinity of the dam is rather complex, the wave is seen to settle down after a while to a rather

stable shape dilating at a constant rate. A strong feature is both series of tests is the steep sediment-laden bore at the front of the wave. The granular velocity pattern shows how material from the downstream bed is swept into the flow as the bore advances.

The Taipei light sediment experiments exhibit one conspicuous flow feature absent from our theoretical description: the hydraulic jump which forms and endures near the centre of the wave. Its distinguishing traits are the non-monotonous free-surface profile, near-surface turbulence and irregular waves radiating energy downstream (Benjamin & Lighthill 1954; Longuet-Higgins 1992). The analysis and numerical results of Capart & Young (1998) indicate that this jump may be due to non-equilibrium sediment transport effects. The upstream flow is unable to instantaneously lower its Froude number by loading itself with sediment. At the wave centre, it meets a higher backwater curve connected to the erosional bore, and wave breaking ensues. The Louvain experiments performed with heavier grains also exhibit an irregular free surface near the wave centre, but to a much lesser degree. This issue is addressed in more detail below.

Before comparing experimental profiles and Riemann solutions, the phenomenological assumptions underlying the proposed theory can first be scrutinized further. The shallow-water approximation does appear applicable. Within a short time after the gate release, the measured velocities roughly align in the horizontal direction. Even where the curvature of the interfaces is strong, the granular motions do not deviate widely from horizontal rectilinear paths. The image sequences shown in figures 12 and 14 also substantiate our postulate of sharp stratification into sediment-free and sediment-rich regions. The time scale of pore pressure dissipation, estimated according to Foda *et al.* (1997), is verified to be faster than the hydrodynamic time scale t_0. Instantaneous pore pressure equilibration is thus a reasonable hypothesis. Finally, to corroborate our assumption of contact-load transport, it is checked that both sets of experiments remain beneath the suspension threshold (Batchelor 1965; Sumer *et al.* 1996).

$$\frac{u_f}{w} < 1, \tag{113}$$

where $u_f = \sqrt{\tau_{bn}/\rho_w}$ = friction velocity and w = particle fall velocity.

5.3. *Comparison of theory and experiments*

Figures 16, 17 and 18 present comparisons between measured interface profiles and shallow-water Riemann solutions. The results are presented in self-similar coordinates and compared with empirical data sampled at different times t/t_0. Results for the Taipei tests are shown on figure 16. Predictions for the scour pattern and transport-layer thickness are seen to be in reasonable agreement with the theory. The predicted thickness, length, and speed of the mature debris snout at the wavefront match the observations quite well. Consistent with expectations, the agreement is seen to improve over time, reflecting the increasing applicability of the shallow-water assumption as the flow spreads out. As pointed out above, the main discrepancy arises in the central region of the wave, where the theory predicts a constant state yet the observations show a hydraulic jump. Further discussion of this discrepancy is provided below.

Results for the Louvain tests are reported on figure 17. The qualitative features of the scour surface, transport layer, and water free surface are well captured. The profiles exhibit both a recognizable central region and a fully developed debris snout at the forefront. A fair correspondence is obtained for the slopes of the simple wave profiles in the two rarefaction regions. Furthermore, this correspondence improves
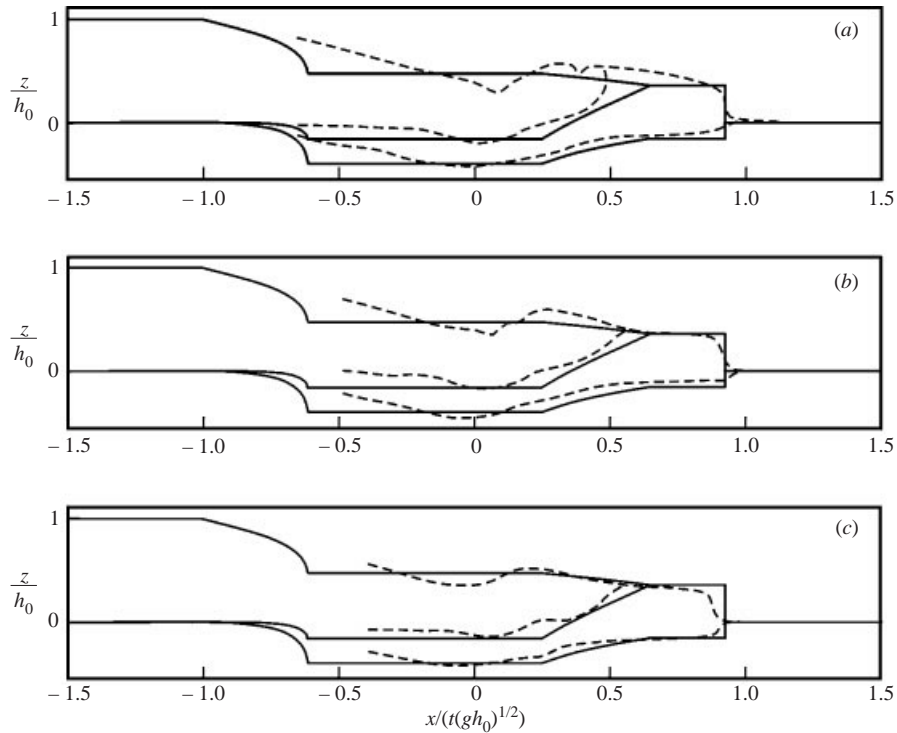
FIGURE 16. Comparison of theoretical (continuous lines) and measured (dashed lines) interface pro-files for the Taipei experiments. Plots in non-dimensional self-similar coordinates with experimental data corresponding to times: (a) $t = 0.3\,\text{s} \approx 3t_0$; (b) $t = 0.4\,\text{s} \approx 4t_0$; (c) $t = 0.5\,\text{s} \approx 5t_0$.

with time. Quantitatively, the thickness of the transport layer is underpredicted. This can be attributed in part to some expansion of the moving granular medium away from static packing, a behaviour not accounted for in the description. A better agreement could also be obtained by calibrating constitutive coefficient C_f separately for the Taipei and Louvain tests. In order to test the general theory under more stringent standards, no such *ad hoc* tuning is performed here. The adopted value $C_f = 0.014$ is calibrated on the basis of the bore thickness observations, averaging best fits to the Taipei and Louvain tests to yield a single constant.

Observations for the Louvain tests further indicate a more localized scour hole, be-lieved to result from memory effects; the gate opening imparts a localized disturbance on the nearby region, which the flow does not completely smooth out as it becomes shallower. An improved experimental device fitted with a less disruptive gate would prove useful in testing this interpretation. Another discrepancy concerns the erosional bore, seen to slow down after some time and lag behind the prediction. Consistent with the reasoning adopted in the scaling analysis, frictional effects appear strongest at the head of the wave. Finally, the free surface does not adopt a completely flat profile in the central region, but rather a rotated S-like shape. These points are further discussed below on the basis of (x, t)-plane comparisons.

For comparison purposes, figure 18 plots results for a purely hydrodynamic dam-break wave. The profiles are reproduced from Stansby, Chegini & Barnes (1998), and concern a water body of depth $h_0 = 10\,\text{cm}$ released upstream of a water layer of depth $h_1 = 0.45h_0$. The Stoker solution (Stoker 1957) to the original shallow-water
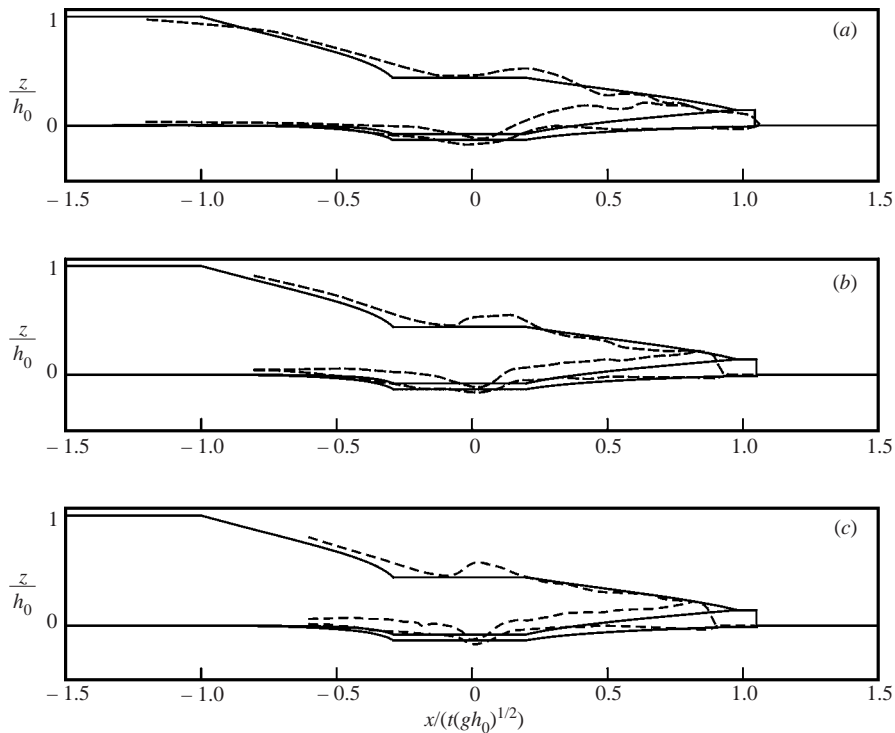
FIGURE 17. Comparison of theoretical (continuous lines) and measured (dashed lines) interface profiles for the Louvain experiments. Plots in non-dimensional self-similar coordinates with experimental data corresponding to times: (a) $t = 0.5\,\text{s} \approx 0.5t_0$; (b) $t = 0.75\,\text{s} \approx 7.5t_0$; (c) $t = 1.00\,\text{s} \approx 10t_0$.

equations derives from a Riemann procedure equivalent to that described above (save for simplifications which arise because the 2×2 system generates only two component waves and because Riemann invariants can be integrated explicitly). The resulting theoretical profile features one rarefaction upstream, a single inner constant state, and a shock-like bore propagating into the downstream water layer. The measurements of Stansby *et al.* (1998) were obtained for conditions very close to those of the present experiments (same initial depth h_0 and similar time range).

Similar discrepancies between theory and experiment are observed in the rigid and erodible bed cases. In both cases, as time progresses, the physical flow adopts a rather sharp profile at the wave front, consistent with the bores of shallow-water theory. Nevertheless, the observed free surfaces tend to smooth out noticeably the cusps predicted by the theory at the bounds of the simple wave regions. These are locations of strong curvature (the cusps imply infinite curvature) where the shallow-water assumption breaks down and non-hydrostatic effects arise. A more rounded negative wave results upstream, then an undershoot where the upstream rarefaction meets the central constant state, then an overshoot further downstream. Non-hydrostatic effects are thus sufficient to prevent the formation of a perfectly flat constant state in the central region of the wave. Other effects likely to intervene as well in the erosional case include non-equilibrium lag in the sediment load, and memory of the gate disturbance etched into the bed profile.

Figure 19 highlights the contrasting behaviours obtained for light and dense sediment materials. For the light material of the Taipei tests, the wave body features a deep transport layer. At the front, this transport layer invades the entire flow
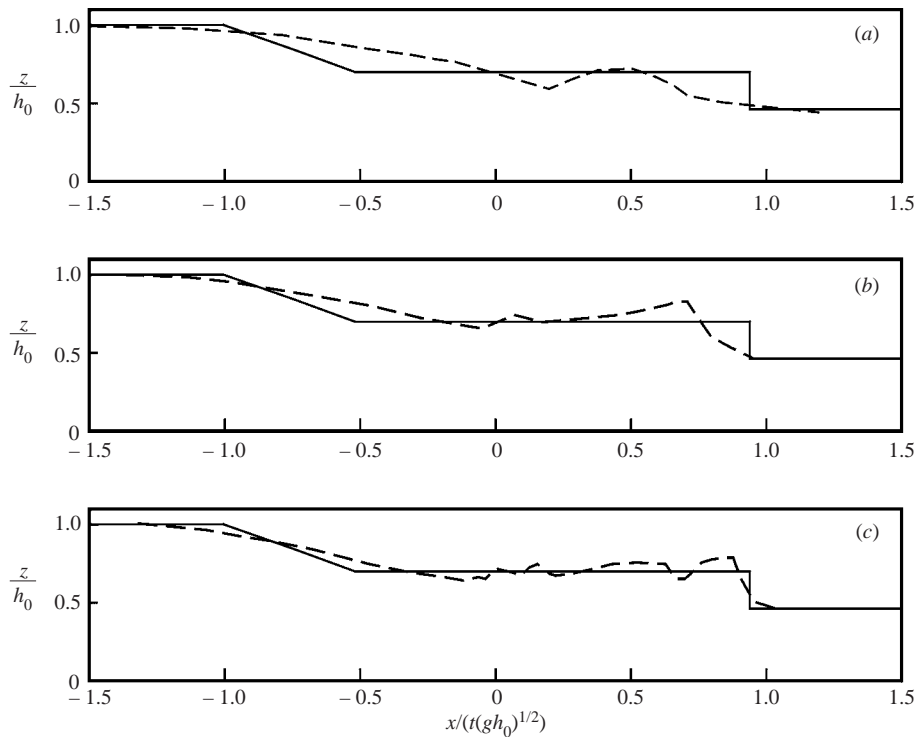
FIGURE 18. Comparison of theoretical (continuous lines) and measured (dashed lines) free-surface profiles for a purely hydrodynamic dam-break wave propagating into a water layer of constant depth $h = 0.45h_0$. Stoker (1957) theoretical solution and experimental data from Stansby *et al.* (1998) obtained for $h_0 = 10\,\text{cm}$ at times (*a*) $t = 0.30\,\text{s} \approx 3t_0$; (*b*) $t = 0.52\,\text{s} \approx 5t_0$; $t = 0.76\,\text{s} \approx 7.5t_0$.

depth, forming a long, thick debris snout. For the denser material of the Louvain tests, by contrast, the transport layer is significantly shallower. A mature debris flow region is still observed at the front, but it is shorter and thinner. Although the transport layer thickness is dependent on the sediment mobility, the speed of the wavefront is not. Depicted on figure 19 at exactly the same instant, the Louvain wavefront is only slightly ahead of its Taipei counterpart. The comparison further shows that the sediment-free water layer retains much the same depth in the light and dense sediment cases. This makes it clear that, for such intense regimes of contact load transport, erosion does not occur so much with water 'picking up' grains from the bed. Rather, the process is one whereby an interface between moving and static regions progresses downward into the bed substrate. This view of the bed boundary as a phase interface lies at the core of the present theoretical description. The Riemann solutions which result are seen in figure 19 to account well for the main features of the observed erosional waves. It should be emphasized that this agreement is obtained with a minimal amount of tuning. The theory involves a single adjustable constitutive constant (friction coefficient C_f) independent of the density ratio.

To complete the comparisons, figure 20 plots the trajectories of wave region boundaries in the non-dimensional (x, t)-plane. Introduced as part of the theoretical description, these boundaries are, of course, not so well defined for the experimental profiles. The sketch in figure 20(*a*) illustrates the manner in which the identification is performed on the basis of the measured interfaces. Boundary x_{LL} corresponding
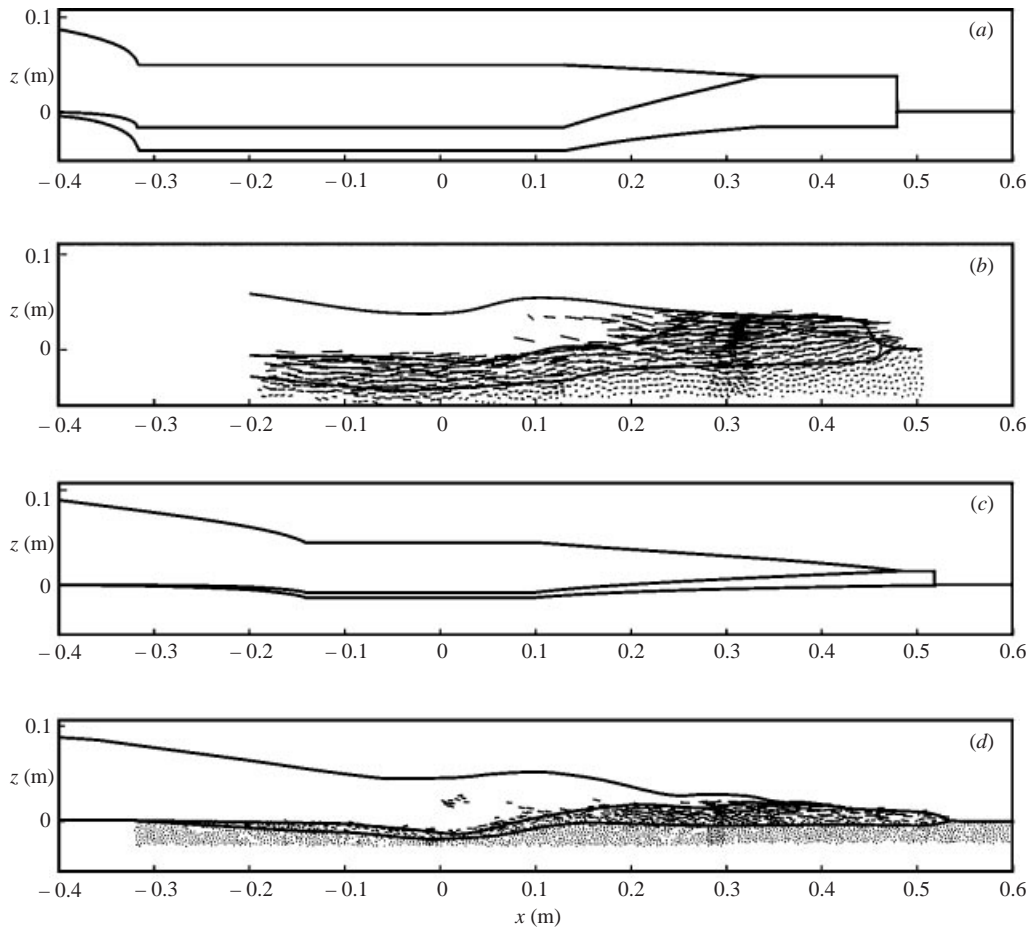
FIGURE 19. Contrast in behaviour observed for sediments of different densities. (*a*), (*b*) Theoretical and experimental results for the conditions of the Taipei tests ($s = \rho_s/\rho_w = 1.048$). (*c*), (*d*) Theoretical and experimental results for the conditions of the Louvain tests ($s = \rho_s/\rho_w = 1.54$). The four sets of results all correspond to time $t = 0.50\,\text{s} \approx 5t_0$.

to the leading edge of the negative wave is chosen as the intersection of the initial water surface with a linear extrapolation from the point of changing curvature in the upstream water profile. Positions x_{LR} and x_{RL} bounding the central constant state are determined by applying an equal areas rule to the rotated S-like profile of the water free surface. The downstream limit x_{RR} of the second rarefaction wave is the point where the sediment interface Γ_s meets the water free surface Γ_w. Finally, the shock position x_S is taken as the point of maximum water surface gradient at the flow front. Some judgement is involved in applying these criteria, and again the estimated positions are not to be taken too literally.

Figure 20(*b*) displays the results for the Taipei tests. A good correspondence between theory and experiments is obtained for three of the region boundaries: x_{LL}, x_{RR} and x_S. The upstream propagation of the negative wave as well as the speed and evolution of the debris snout at the front thus appear to be captured well by the description. The comparison is much worse for the boundaries x_{LR} and x_{RL} of the central state, indicating that the description is qualitatively deficient in this region. As
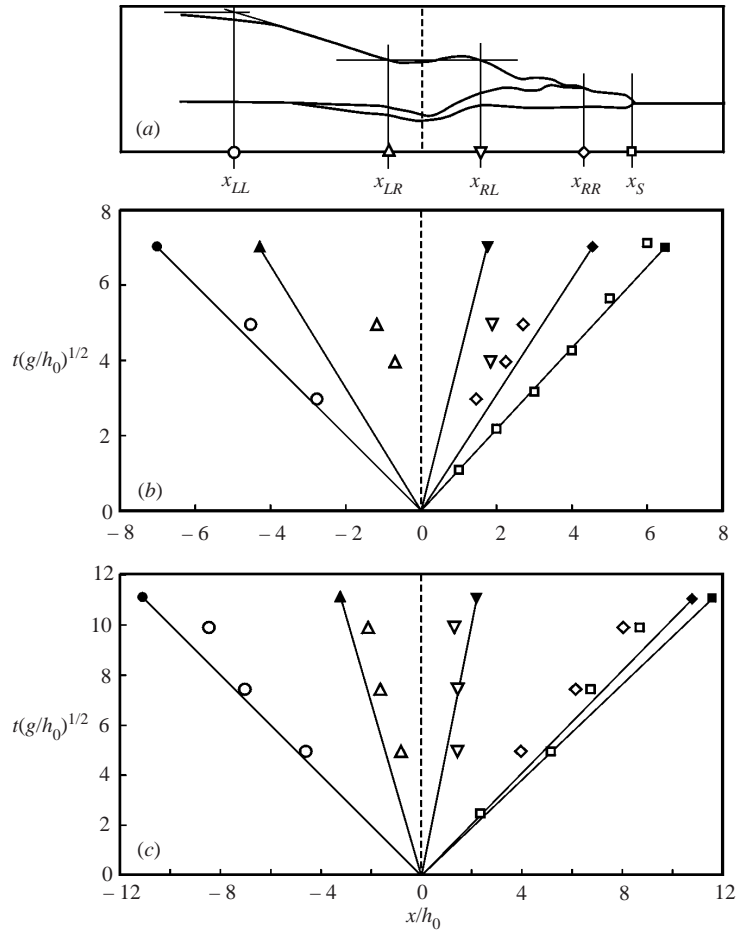
FIGURE 20. Comparison of theory and experiments for the (x, t)-paths of the wave region boundaries: (*a*) definition sketch for the empirical identification of region boundaries; (*b*) theoretical (lines and filled symbols) and experimental (hollow symbols) paths for the Taipei tests; (*c*) theoretical (lines and filled symbols) and experimental (hollow symbols) paths for the Louvain tests.

discussed above and analysed in more depth in Capart & Young (1998), the culprit is the strong hydraulic jump forming at the wave centre. For the light material of the Taipei tests, the equilibrium transport assumption is not justified in the observed time range. As shown by the numerical computations of Capart & Young (1998), taking non-equilibrium lag into account suffices to capture the jump formation qualitatively. It is nonetheless very likely that non-hydrostatic pressure effects contribute as well. The same non-equilibrium computational results predict a front profile very similar to that obtained in the present equilibrium theory (save for a slightly smoother transition). It therefore appears that the central wave region is the most sensitive to non-equilibrium behaviour.

Results for the Louvain tests are shown on figure 20(*c*). For these tests, a fair agreement is observed for all the boundary paths including the limits x_{LR} and x_{RL} of the central constant state. This confirms the expectations of the scaling analysis. The Louvain tests approximate more closely the conditions of validity of the present description. The qualitative changes in wave structure observed when going from light

material to dense material experiments are also well captured by the theory. This is the case in particular for the distance $x_S - x_{RR}$ which measures the extent of the mature debris snout region at the wavefront. The distance is much smaller for the dense material Louvain tests than for the light material Taipei experiments, a trend which is accurately predicted.

As time progresses, the experimental wave paths are observed to gradually curve inwards. This deviation from the constant rate of expansion predicted by the theory reflects the influence of additional dissipative effects. For the Louvain tests, the observed deceleration appears consistent with the time scale $t_f \sim 20t_0$ over which frictional momentum losses are expected to make their influence felt. For the Taipei tests, on the other hand, the deceleration occurs sooner than anticipated on the basis of the time scale analysis of §3.3. Examination of the experimental footage and further experiments with the Taipei material (Triadantasio 1999) show that another process intervenes at around $t \sim 10t_0$. At this point, the water and granular phases unlock from each other, and a seepage wave escapes ahead of the slower granular surge. Regardless of the physical mechanism, time $t \sim 10t_0$ appears to be an effective limit of validity of the present description, beyond which the wave starts to adopt a diffusive rather than inertial behaviour.

6. Summary and conclusions

The present paper proposes an approximate theoretical description of the formative stages of erosional dam-break flows. The description is based on a shallow-water approach extended to fast geomorphic phenomena. At its core lies a view of the mobile bed boundary as an evolving phase interface across which saturated granular material undergoes a transition from solid- to fluid-like behaviour. Closure of the equations is achieved by invoking familiar principles from hydraulics and soil mechanics. Reduced to a homogeneous system of hyperbolic equations, the framework becomes tractable by the Riemann techniques of gas dynamics. Self-similar solutions expanding at a constant rate are obtained for the dam-break problem. The wave structure for the erosional dam-break flow features two inner regions of uniform flow, two centred simple waves and a shock wave. Sudden bulking of the flow with eroded sediment involves a key dynamical effect absent from classical alluvial hydraulic descriptions; the inertia of the eroded material decelerates the flow and shapes its forefront into a steep debris snout. The theoretical description is compared to two sets of experimental results obtained for sediment materials of low and intermediate densities. By imaging the flows with digital cameras and visualizing the granular motions with particle-tracking techniques, detailed pictures of the wave patterns are acquired. These make it possible to substantiate the constitutive assumptions of the theory as well as test its predictions. With minimal tuning (a single constitutive constant), fair agreement is obtained between theory and experiment. Most of the features of the observed profiles are reasonably captured, and the contrast in behaviour between light and dense sediments is anticipated well. The window $t \sim [5t_0 \ 10t_0]$ (where $t_0 = t(g/h_0)^{1/2}$ is the hydrodynamic time scale) delineates an approximate domain of applicability of the present description. Within that window, the agreement recorded is on a par with comparisons between rigid-bed experiments and the Stoker theoretical solution. Beyond this range, however, frictional momentum dissipation or seepage phenomena begin to take over, and a transition to diffusive behaviour is to be expected. Investigation of the long time behaviour is believed to be a fruitful avenue for further work.

The authors gratefully acknowledge the support of the following people and institutions. H. C. benefited from the hospitality of the Università degli Studi di Trento and L. F. from the hospitality of the Université catholique de Louvain. Professors A. Armanini, E. F. Toro, D. L. Young and Y. Zech, the editor Professor D. H. Peregrine and anonymous reviewers made insightful objections and suggestions. M. Larcher and L. Guarino in Trento, R. Solar, J.-L. Van Goethem and L. Villers in Louvain-la-Neuve and Y. H. Liu in Taipei contributed to the exploratory stages of the experimental work. Special thanks are extended to B. Spinewine who prepared and carried out the Louvain laboratory tests.

REFERENCES

ABBOTT, M. B. 1979 *Computational Hydraulics. Elements of the Theory of Free Surface Flows.* Pitman.

ADRIAN, R. J. 1991 Particle-imaging techniques for experimental fluid mechanics. *Annu. Rev. Fluid Mech.* **23**, 261–304.

AHARONOV, E. & SPARKS, D. 2000 Rigidity phase transition in granular packings. *Phys. Rev.* E **60**, 6890–6896.

ALCRUDO, F., GARCIA-NAVARRO, P. & SAVIRON, J. M. 1992 Flux difference splitting for 1D open channel flow equations. *Intl J. Numer-Meth. Fluids* **14**, 1009–1018.

ARMANINI, A. & DI SILVIO, G. 1988 A one-dimensional model for the transport of a sediment mixture in non-equilibrium conditions. *J. Hydraul. Res.* **26**, 275–292.

ARMANINI, A. & FRACCAROLLO, L. 1997 Critical conditions for debris flows. In C. L. Chen (ed.), *Proc. 1st Intl Conf. on Debris-Flow Hazards Mitigation, San Francisco (August 1997)*, pp. 434–443. ASCE.

ARMANINI, A., FRACCAROLLO, L., GUARINO, L., MARTINO, R. & BIN, Y. 2000 Experimental analysis of the general features of uniform debris-flow over a loose bed. In G. F. Wieczorek & N. D. Naeser (ed.), *Proc. 2nd Intl Conf. on Debris-Flow Hazards Mitigation, Taipei, Taiwan (August 2000)*, pp. 327–334. Balkema.

ASANO, T. 1995 Sediment transport under sheet-flow conditions. *J. Waterways Port Coast. Ocean Engng* **121**, 239–246.

BAGNOLD, R. A. 1954 Experiments on a gravity-free dispersion of large solid spheres in a Newtonian fluid under shear. *Proc. R. Soc. Land.* A **255**, 49–63.

BATCHELOR, G. K. 1965 The motion of small particles in turbulent flow. *Proc. 2nd Australian Conf. on Hydraul. and Fluid Mech. Univ. of Auckland, Auckland, Australia*, pp. 019–041.

BENITO, G., GRODEK, T. & ENZEL, Y. 1998 The geomorphic and hydrologic impacts of the catastrophic failure of flood-control dams during the 1996-Biescas flood (Central Pyrenees, Spain). *Z. Geomorph*, **42**, 417–437.

BENJAMIN, T. B. & LIGHTHILL, M. J. 1954 On cnoidal waves and bores. *Proc. R. Soc. Lond.* A **224**, 448–460.

BROOKS, G. R. & LAWRENCE, D. E. 1999 The drainage of Lake Ha! Ha! reservoir and downstream geomorphic impacts along Ha! Ha! River, Saguenay area, Quebec, Canada. *Geomorphology* **28**, 141–168.

CAPART, H. 2000 Dam-break induced geomorphic flows and the transition from solid- to fluid-like behaviour across evolving interfaces. PhD thesis, University Catholique de Louvain, Belgium.

CAPART, H., FRACCAROLLO, L., GUARINO, L., ARMANINI, A. & ZECH, Y. 2000 Granular temperature behaviour of loose bed debris flows. In G. F. Wieczorek & N. D. Naeser (ed.), *Proc. 2nd Intl Conf. on Debris-Flow Hazards Mitigation, Taipei, Taiwan (August 2000)*, pp. 361–368. Balkema.

CAPART, H. & YOUNG, D. L. 1998 Formation of a jump by the dam-break wave over a granular bed. *J. Fluid Mech.* **372**, 165–187.

CAPART, H., YOUNG, D. L. & ZECH, Y. 2002 Voronoï imaging methods for the measurement of granular flows. *Exps. Fluids* **32**, 121–135.

CHAPMAN, C. J. 2000 *High Speed Flow.* Cambridge University Press.

CHEN, Y. H. & SIMONS, D. B. 1979 An experimental study of hydraulic and geomorphic changes in an alluvial channel induced by failure of a dam. *Water Resources Res.* **15**, 1183–1188.

CHOW, V. T. 1973 *Open-channel Hydraulics*. McGraw–Hill.

CLAGUE, J. J., EVANS, S. G. & BLOWN, I. G. 1985 A debris flow triggered by the breaching of a moraine-dammed lake, Klattasine Creek, British Columbia. *Canad. J. Earth Sci.* **22**, 1492–1502.

COSTA, J. E. & SCHUSTER, R. L. 1988 The formation and failure of natural dams. *Bull. Geol. Soc. Am.* **100**, 1054–1068.

DANIEL, S. M. 1965 Flow of suspensions in a rectangular channel. PhD thesis, University of Saskatchewan, Canada.

DRESSLER, R. F. 1954 Comparison of theories and experiments for the hydraulic dambreak wave. In *Assemblée Général de Rome*, vol. 3, pp. 319–328. Intl Assoc. of Hydrology.

FENNEMA, R. J. & CHAUDHRY, M. H. 1987 Simulation of one-dimensional dam-break flows. *J. Hydraul. Res.* **25**, 41–51.

FODA, M. A., HILL., D. F., DeNEALE, P. L. & HUANG, C. M. 1997 Fluidization response of sediment bed to rapidly falling water surface. *J. Waterways Port Coast. Ocean Engng* **123**, 261–265.

FRACCAROLLO, L. & TORO, E. F. 1995 Experimental and numerical assessment of the shallow water model for two-dimensional dam-break type problems. *J. Hydraul. Res.* **33**, 843–864.

GALAPPATTI, R. & VREUGDENHIL, C. B. 1985 A depth-integrated model for suspended sediment transport. *J. Hydraul. Res.* **23**, 359–377.

GALLINO, G. L. & PIERSON, T. C. 1985 Pollalie Creek debris flow and subsequent dam-break flood of 1980, East Fork Hood River Basin, Oregon. *US Geol. Survey Water Supply Paper* 2273, 22 pp.

GLAISTER, P. 1988 Approximate Riemann solutions of the shallow water equations. *J. Hydraul. Res.* **26**, 293–306.

HANES, D. M. & BOWEN, A. J. 1985 A granular–fluid model for steady intense bed-load transport. *J. Geophys. Res.* **90**, 9149–9158.

HOLLY, F. M. JR & RAHUEL, J. L. 1990 New numerical/physical framework for mobile-bed modelling, Part I – Numerical and physical principles. *J. Hydraul. Res.* **27**, 401–416.

HUNGR, O. 1995 A model for the runout analysis of rapid flow slides, debris flows, and avalanches. *Can. Geotech. J.* **32**, 610–623.

INRS-EAU 1997 Simulation hydrodynamique et bilan sédimentaire des rivières Chicoutimi et des Ha! Ha! suite aux crues exceptionnelles de juillet 1996. *INRS-Eau Rep.* R487, 207 pp.

IVERSON, R. M. 1997 The physics of debris flows. *Rev. Geophys.* **35**, 245–296.

IVERSON, R. M. & LaHUSEN, R. G. 1989 Dynamic pore-pressure fluctuations in rapidly shearing granular materials. *Science* **246**, 796–798.

JARRETT, R. D. & COSTA, J. E. 1986 *Hydrology, Geomorphology and Dam-Break Modeling of the July 15, 1982 Lawn Lake Dam and Cascade Lake Dam Failures, Larimer County, Colorado*. U.S. Government Printing Office, Washington, 78 pp.

JEFFREY, A. 1976 *Quasilinear Hyperbolic Systems and Waves*. Pitman.

JENKINS, J. T. & ASKARI, E. 1991 Boundary conditions for rapid granular flows: phase interfaces. *J. Fluid Mech.* **223**, 497–508.

JENKINS, J. T. & HANES, D. M. 1998 Collisional sheet-flow of sediment driven by a turbulent fluid. *J. Fluid Mech.* **370**, 29–52.

JENKINS, J. T. & SAVAGE, S. B. 1983 A theory for the rapid flow of identical, smooth, nearly elastic particles. *J. Fluid Mech.* **130**, 187–207.

LAI, C. 1991 Modelling alluvial channel flow by multimode characteristic method. *J. Engng Mech.* **117**, 32–53.

LAMBE, T. W. & WHITMAN, R. V. 1969 *Soil Mechanics*. Wiley.

LAPOINTE, M. F., SECRETAN, Y., DRISCOLL, S. N., BERGERON, N. & LECLERC, M. 1998 Response of the Ha! Ha! River to the flood of July 1996 in the Saguenay Region of Quebec: large-scale avulsion in a glaciated valley. *Water Resources Res.* **34**, 2383–2392.

LAX, P. 1957 Hyperbolic systems of conservation laws II. *Commun. Pure Appl. Maths* **10**, 537–566.

LEAL, J. & FERREIRA, R. 1999 One-dimensional mathematical modelling of the instantaneous dam-break flood wave over mobile bed: application of second order TVD schemes and first-order flux-splitting schemes. In *Proc. Concerted Action on Dam-break Modelling Munich Workshop*. CADAM.

LONGUET-HIGGINS, M. S. 1992 Capillary rollers and bores. *J. Fluid Mech.* **240**, 659–679.

MORRIS, P. H. & WILLIAMS, D. J. 1996 Relative celerities of mobile bed flows with finite solids concentrations. *J. Hydraul. Engng* **122**, 311–315.

NNADI, F. N. & WILSON, K. C. 1992 Motion of contact-load particles at high shear stress. *J. Hydraul. Engng* **118**, 1670–1684.

PHILLIPS, B. & SUTHERLAND, A. J. 1989 Spatial lag effects in bed load sediment transport. *J. Hydraul. Res.* **27**, 115–133.

RIBBERINK, J. S. & AL-SALEM, A. 1990 Bedforms, sediment concentration and sediment transport in simulated wave conditions. In *Proc. 22nd Intl Coastal Engng Conf* (ed. B. L. Edge), pp. 2318–2331. ASCE.

RITTER, A. 1892 Die fortpflanzung der wasserwellen. *Z. Deut. Ing.* **36**, 947–954.

SAIEDI, S. 1997 A coupled modeling of alluvial flows. *J. Hydraul. Engng* **123**, 440–446.

SAUREL, R. & ABGRALL, R. 1999 A multiphase Godunov method for compressible multifluid and multiphase flows. *J. Comput. Phys.* **150**, 425–467.

STANSBY, P. K., CHEGINI, A. & BARNES, T. C. D. 1998 The initial stages of dam-break flow. *J. Fluid Mech.* **374**, 407–424.

STOKER, J. J. 1957 *Water Waves*. Wiley-Interscience.

STRANG, G. 1968 On the construction and comparison of difference schemes. *SIAM J. Numer. Anal.* **5**, 506–517.

SUMER, B. M., KOZAKIEWICZ, A., FREDSØE, J. & DEIGAARD, R. 1996 Velocity and concentration profiles in sheet-flow layer of movable bed. *J. Hydraul. Engng* **122**, 549–558.

TAKAHASHI, T. 1991 *Debris Flow*. IAHR Monograph. Balkema.

TAKAHASHI, T. & NAKAGAWA, H. 1994 Flood/debris flow hydrograph due to the collapse of a natural dam by overtopping. *J. Hydrosc. Hydraul. Engng* **12**, 41–49.

TORO, E. F. 1989 *Riemann Solvers and Numerical Methods for Fluid Dynamics*. Springer.

TORO, E. F. 1992 Riemann problems and the WAF method for solving the two-dimensional shallow water equations. *Phil. Trans. R. Soc. Lond.* A **338**, 43–68.

TRIADANTASIO, F. 1999 Transport d'une granulométrie bimodale par l'onde de rupture de barrage. B. Engng thesis, University catholique de Louvain, Belgium.

TSUBAKI, T. & SAITO, T. 1967 Regime criteria for sand waves in erodible bed channels. Kyushu University, Faculty of Engineering, *Annuals* **40**, 741–748.

DE VRIES, M. 1965 Considerations about non-steady bed-load transport in open channels. *Proc. XI IAHR Congr.* vol. 3, paper 3.8.

WAYTHOMAS, C. F., WALDER, J. S., MCGIMSEY, R. G. & NEAL, C. A. 1996 A catastrophic flood caused by drainage of a caldera lake at Aniakchak Volcano, Alaska, and implications for volcanic hazards assessment. *Bull. Geol. Soc. Am.* **108**, 861–871.

WHITE, F. M. 1999 *Fluid Mechanics*. McGraw–Hill.

WHITHAM, G. B. 1974 *Linear and Non-linear Waves*. Wiley.

YEGANEH BAKHTIARY, A. & ASANO, T. 1998 Effects of particle properties on oscillatory sheet-flow dynamics. *JSCE Coastal Engng J.* **40**, 61–80.

ZANRÉ, D. D. L. & NEEDHAM, D. J. 1994 On the hyperbolic nature of the equations of alluvial river hydraulics and the equivalence of stable and energy dissipating shocks. *Geophys. Astrophys. Fluid Dyn.* **76**, 193–222.

ZHANG, Y. & CAMPBELL, C. S. 1992 The interface between fluid-like and solid-like behaviour in two-dimensional granular flows. *J. Fluid Mech.* **237**, 541–568.